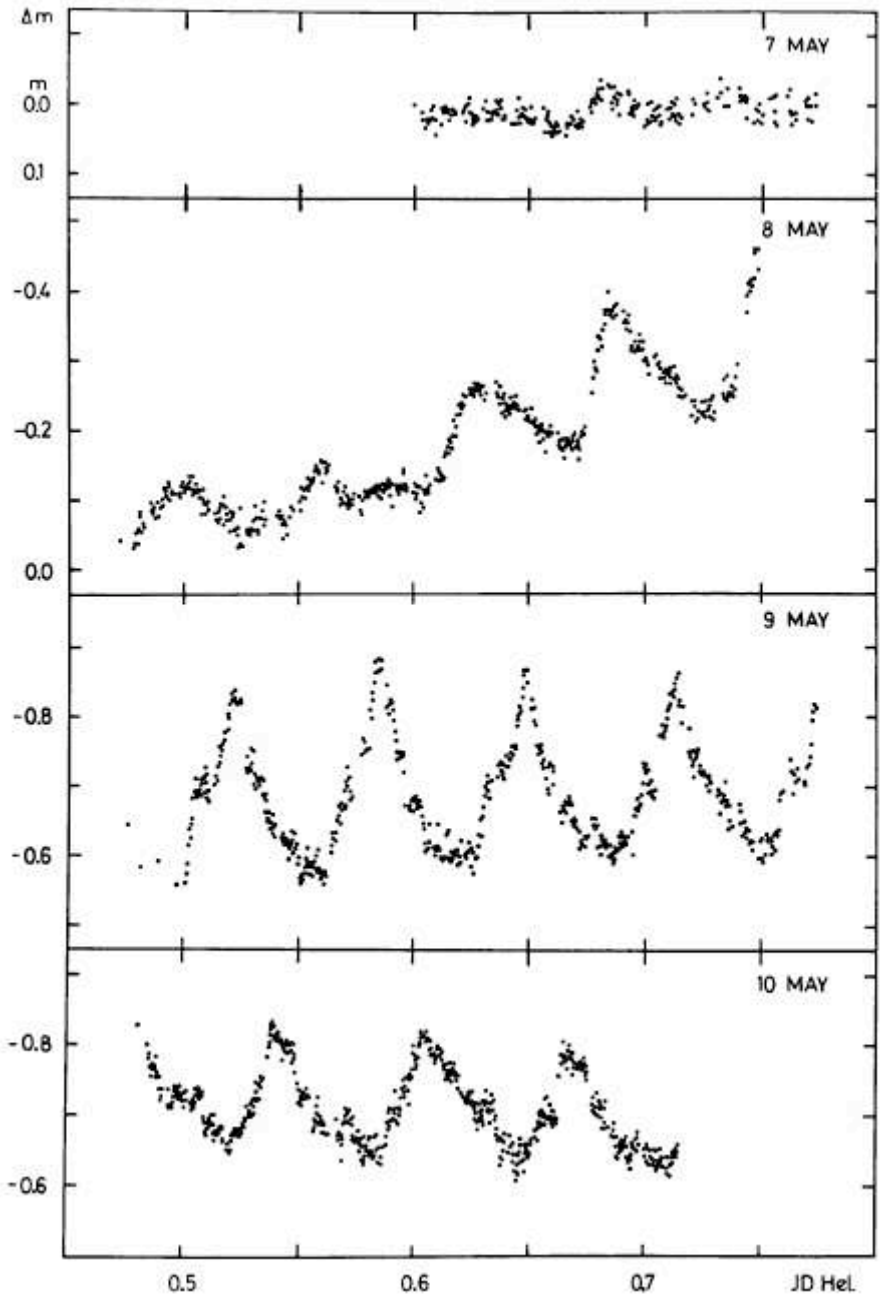
Δm
7 MAY
0.0
0.1
8 MAY
-0.4
-0.2
0.0
9 MAY
-0.8
-0.6
10 MAY
-0.8
-0.6
0.5
0.6
0.7
JD Hel.

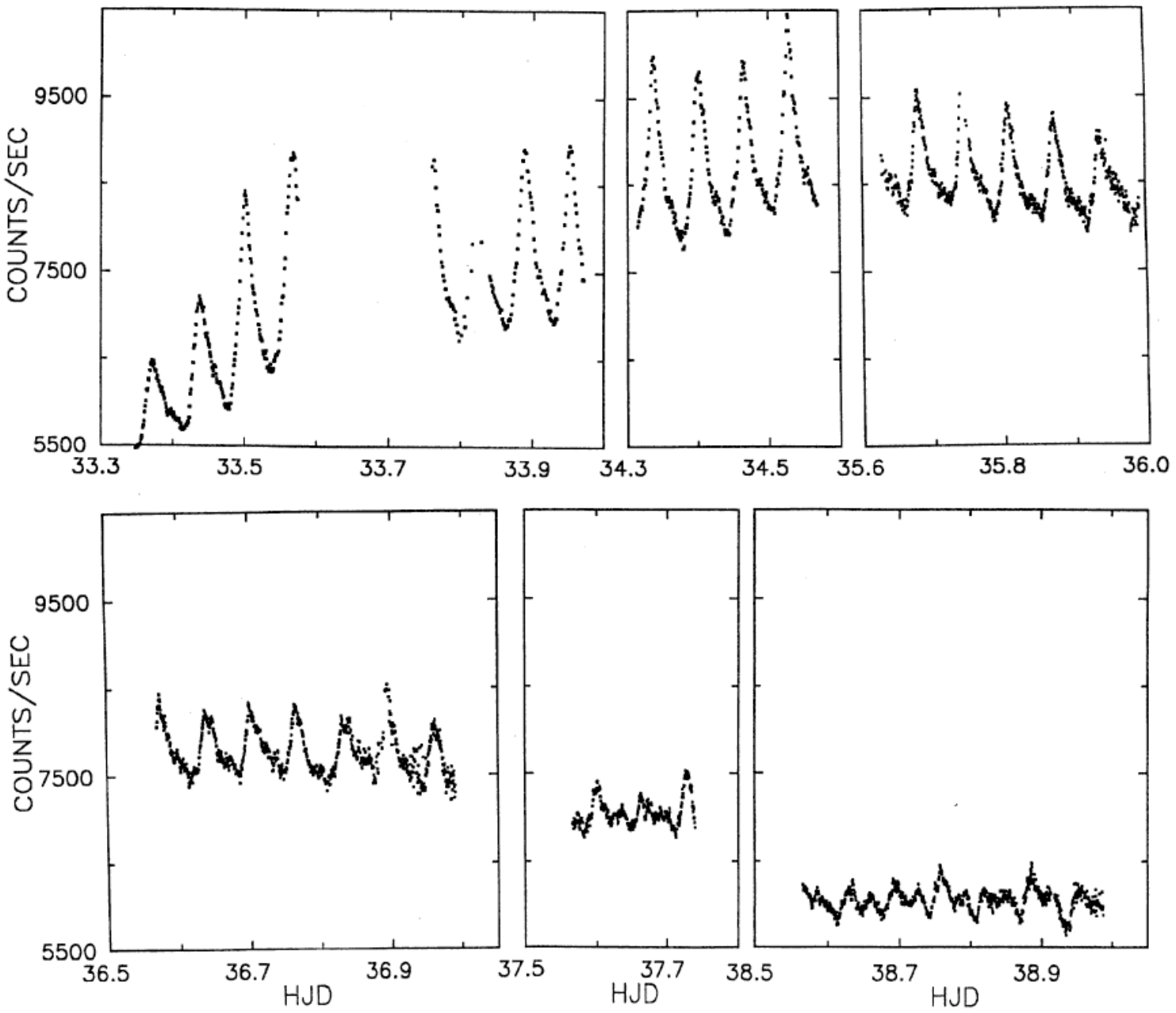
9500
7500
5500
COUNTS/SEC
33.3
33.5
33.7
33.9
34.3
34.5
35.6
35.8
36.0
9500
7500
5500
COUNTS/SEC
36.5
36.7
36.9
HJD
37.5
37.7
HJD
38.5
38.7
38.9
HJD

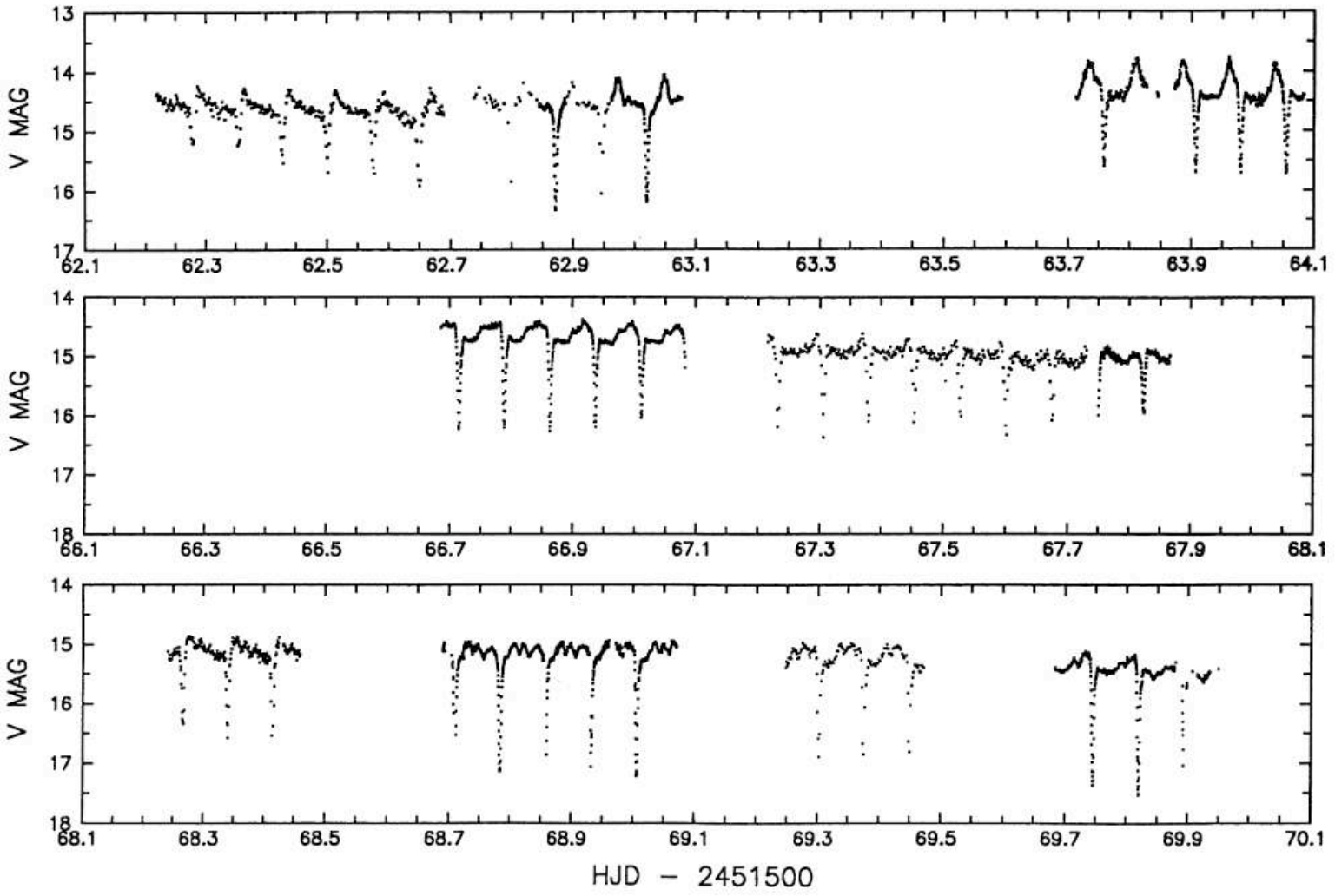


FIG. 2.—Three 48 hour segments of IY UMa light curve during the 2000 January superoutburst. Deep eclipses at $P_{orb}$ occur throughout. A prominent wave, the superhump, drifts slowly through the orbital light curve. The superhump amplitude and eclipse depth are periodically reduced when the superhump coincides with eclipse. Recurrent wiggles at higher frequency are also evident, especially in the last panel.

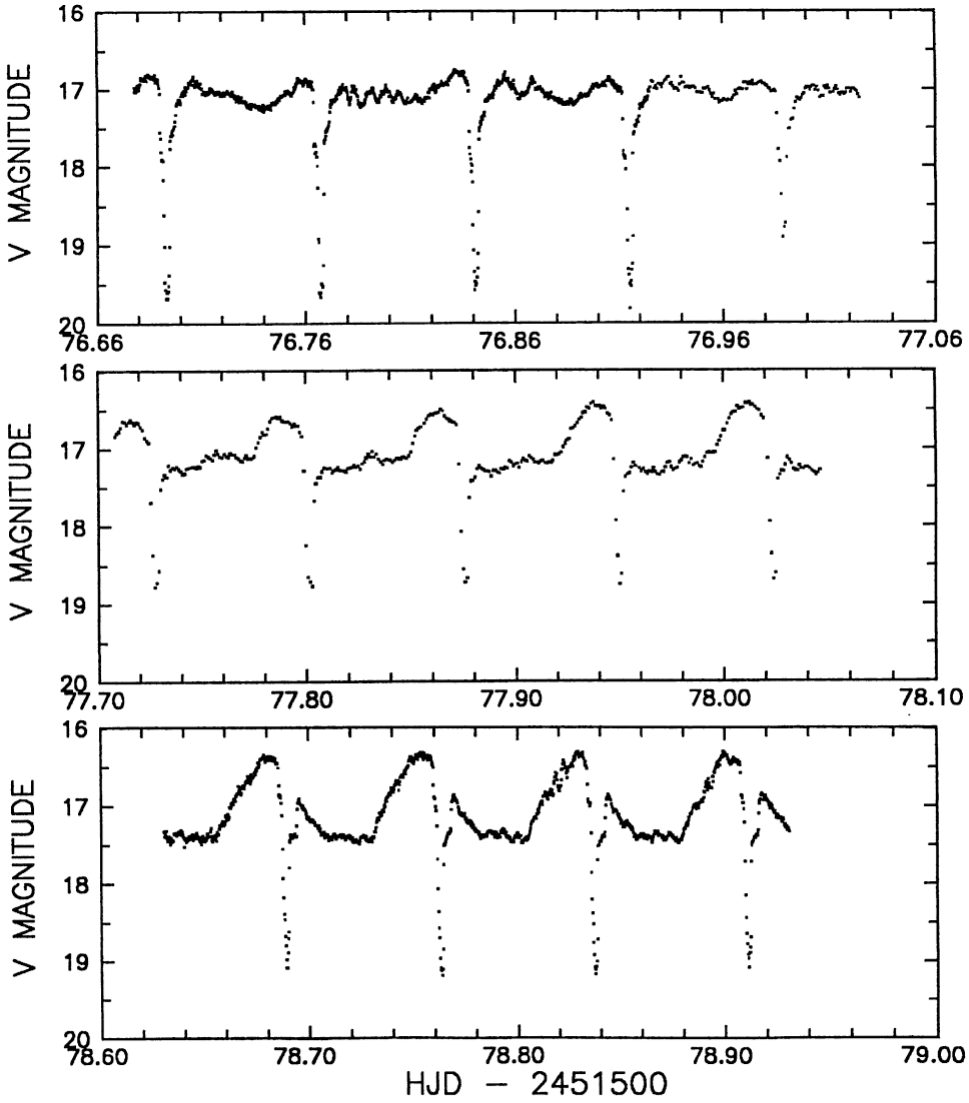


FIG. 4.—Nightly light curves of IY UMa after the rapid decline. A large wave of highly variable amplitude still exists. The eclipses are narrower, deeper, nd sharper, with the sharpest features resolving the size and location of the white dwarf and hot spot.

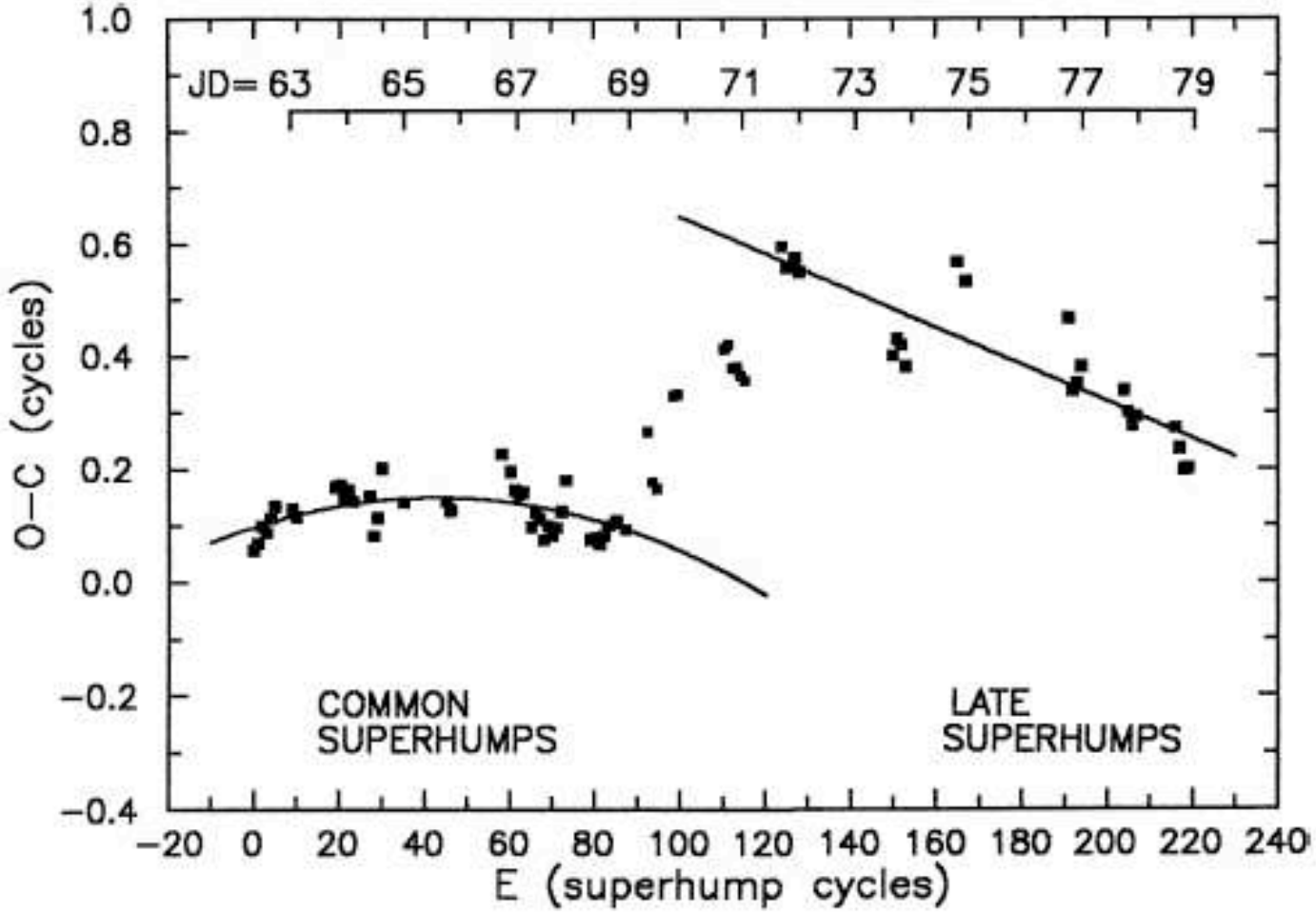
JD= 63
65
67
69
71
73
75
77
79
1.0
0.8
0.6
0.4
0.2
0.0
−0.2
−0.4
O−C (cycles)
COMMON
SUPERHUMPS
LATE
SUPERHUMPS
−20
0
20
40
60
80
100
120
140
160
180
200
220
240
E (superhump cycles)

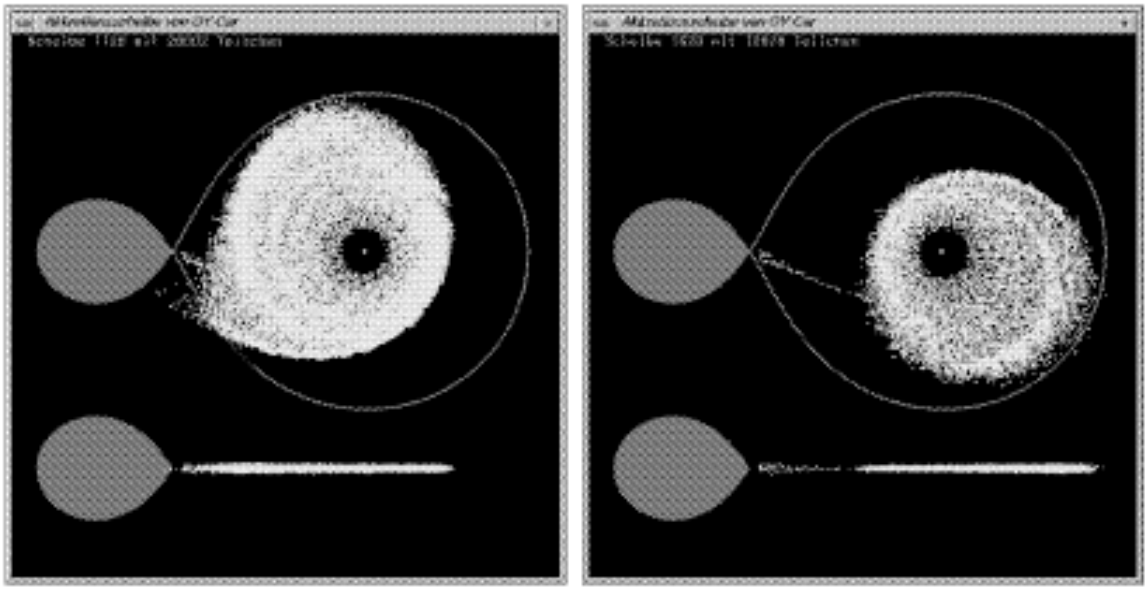

Figure 1. The disk at superhump maximum. **Left:** During superoutburst. **Right:** After decline from superoutburst. During superoutburst, the brightness variations are caused by the viscous dissipation due to the tidal stresses from the secondary. In the late superhump era, the brightness of the stream disk interaction region changes with its distance from the white dwarf.

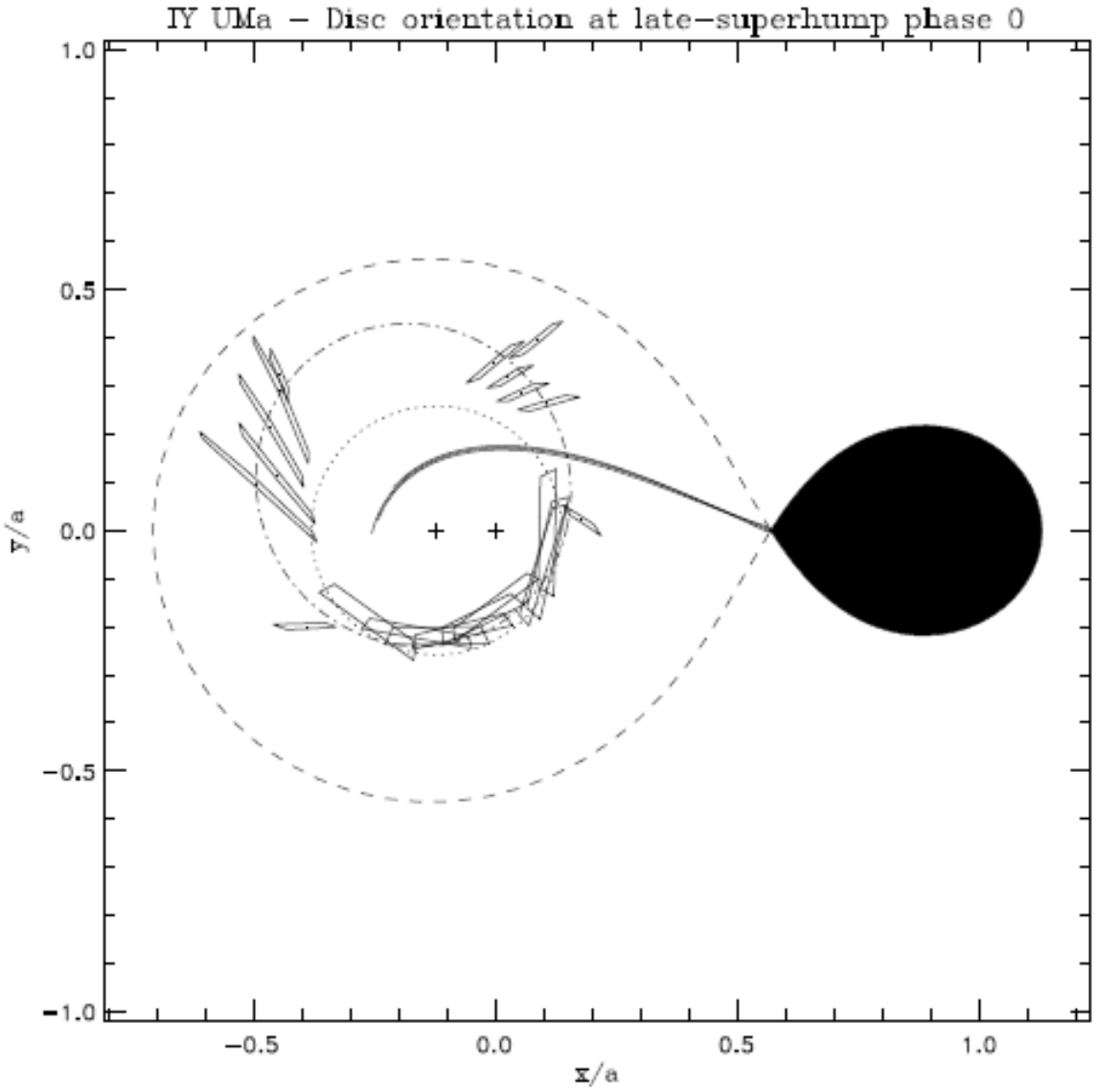
IY UMa - Disc orientation at late-superhump phase 0
1.0
0.5
0.0
−0.5
−1.0
y/a
−0.5
0.0
0.5
1.0
x/a

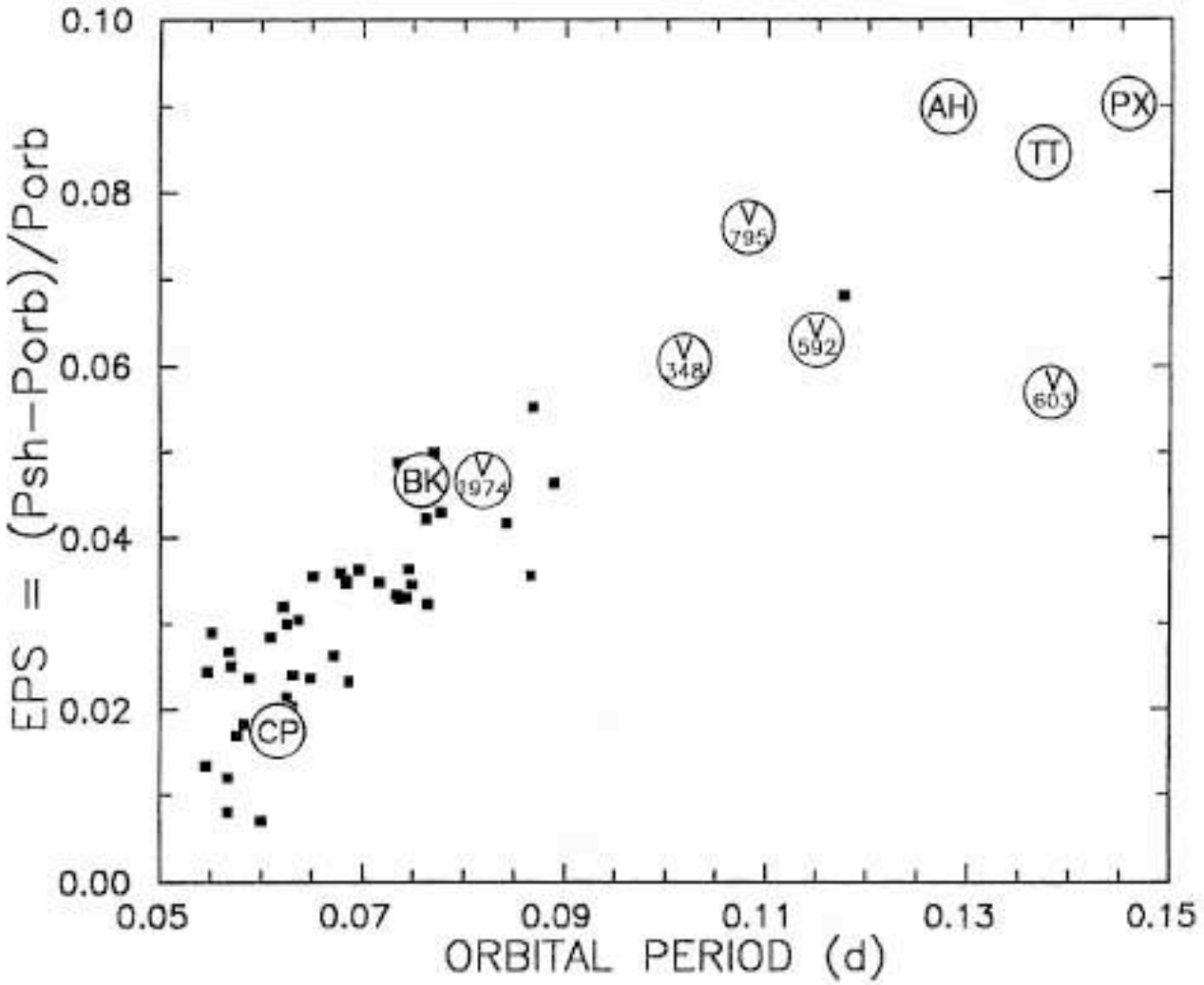


FIG. 3.—The $\epsilon$-$P$ relation for positive superhumpers. SU UMa stars are shown by squares, while permanent superhumpers are labeled by name. Generally $\epsilon$ scales with $P$, but there are a few low points at very short period. Error bars are given in Table 1 and are comparable to the symbol size.

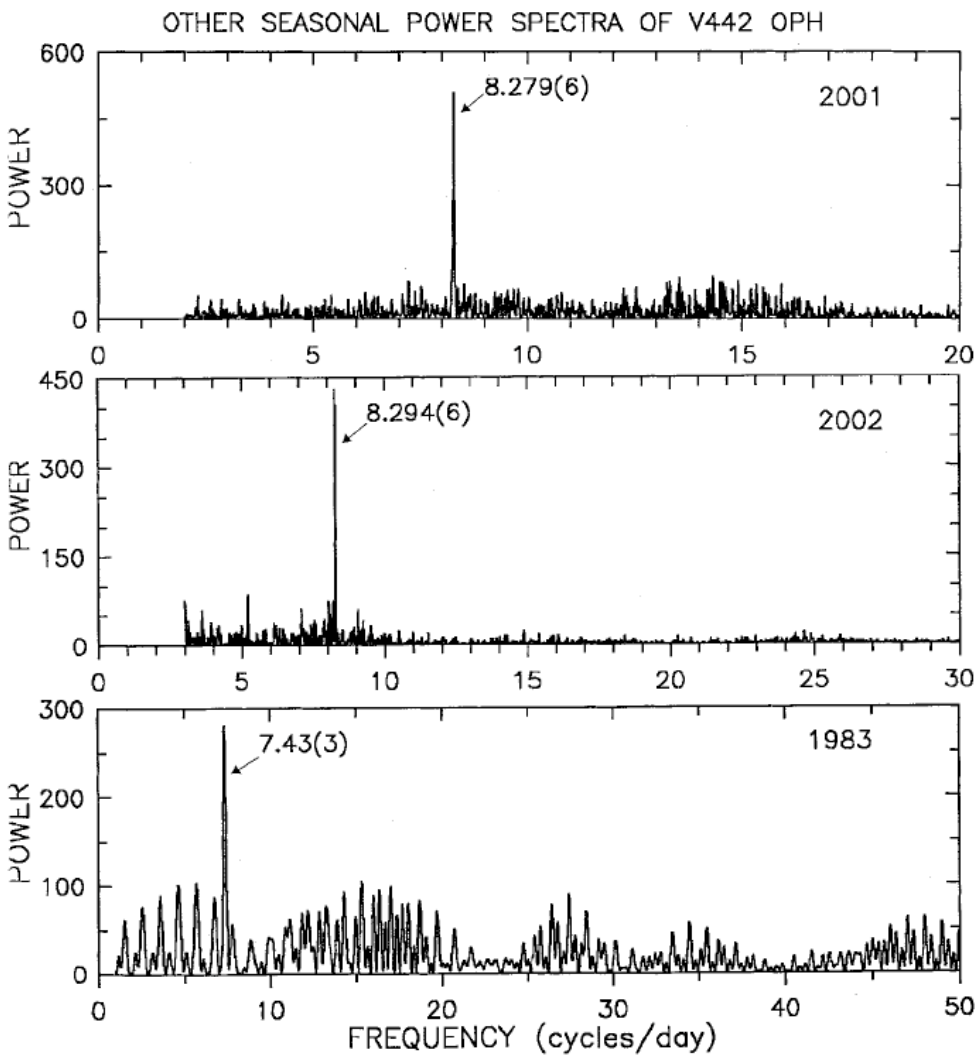


FIG. 9.—Other seasonal power spectra of V442 Oph, cleaned for the aliases of the strongest signal. The negative superhump dominated in 1995, 2001, and 2002; but the 1983 result suggests a possible apsidal superhump.

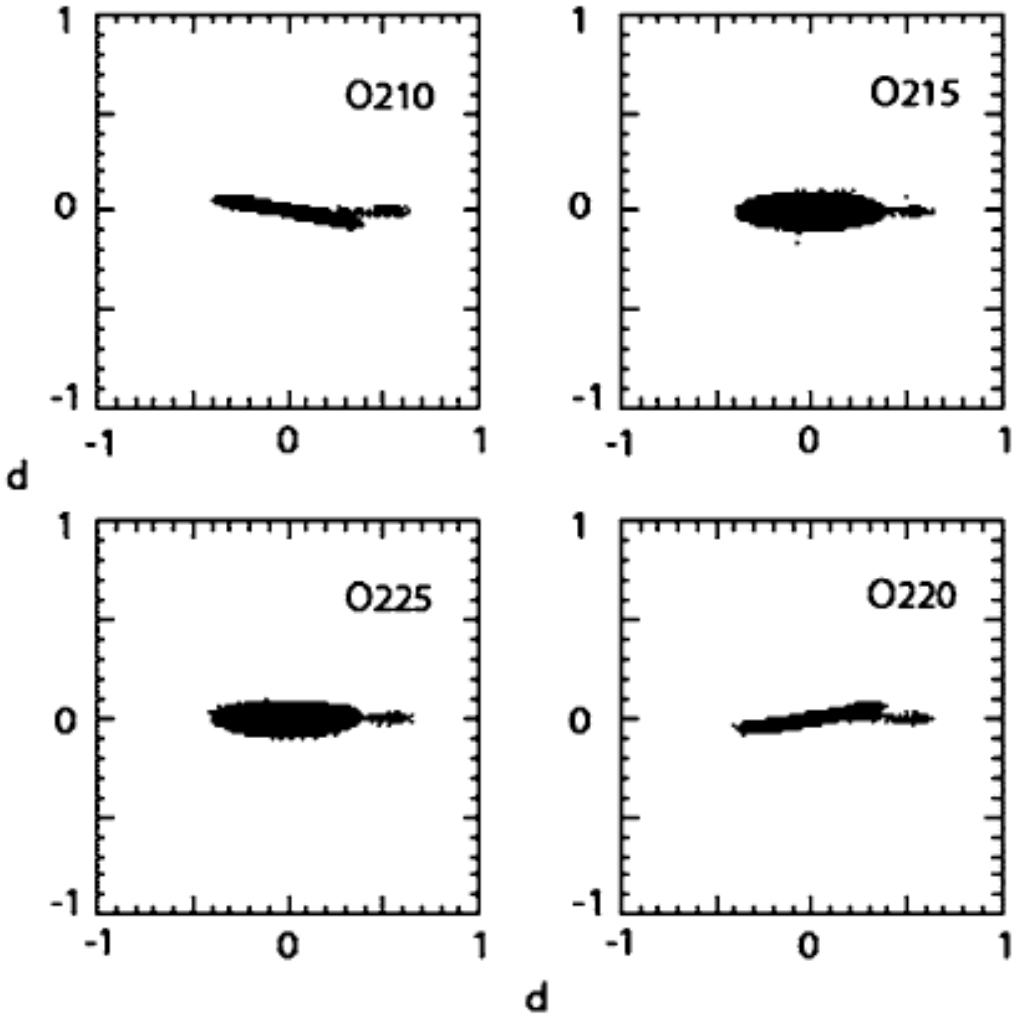


**Figure 5.** Retrograde precession of a disk fully tilted 5° around the line of nodes, out of the orbital plane, showing that a fully tilted, precessing disk can look like a warped disk.

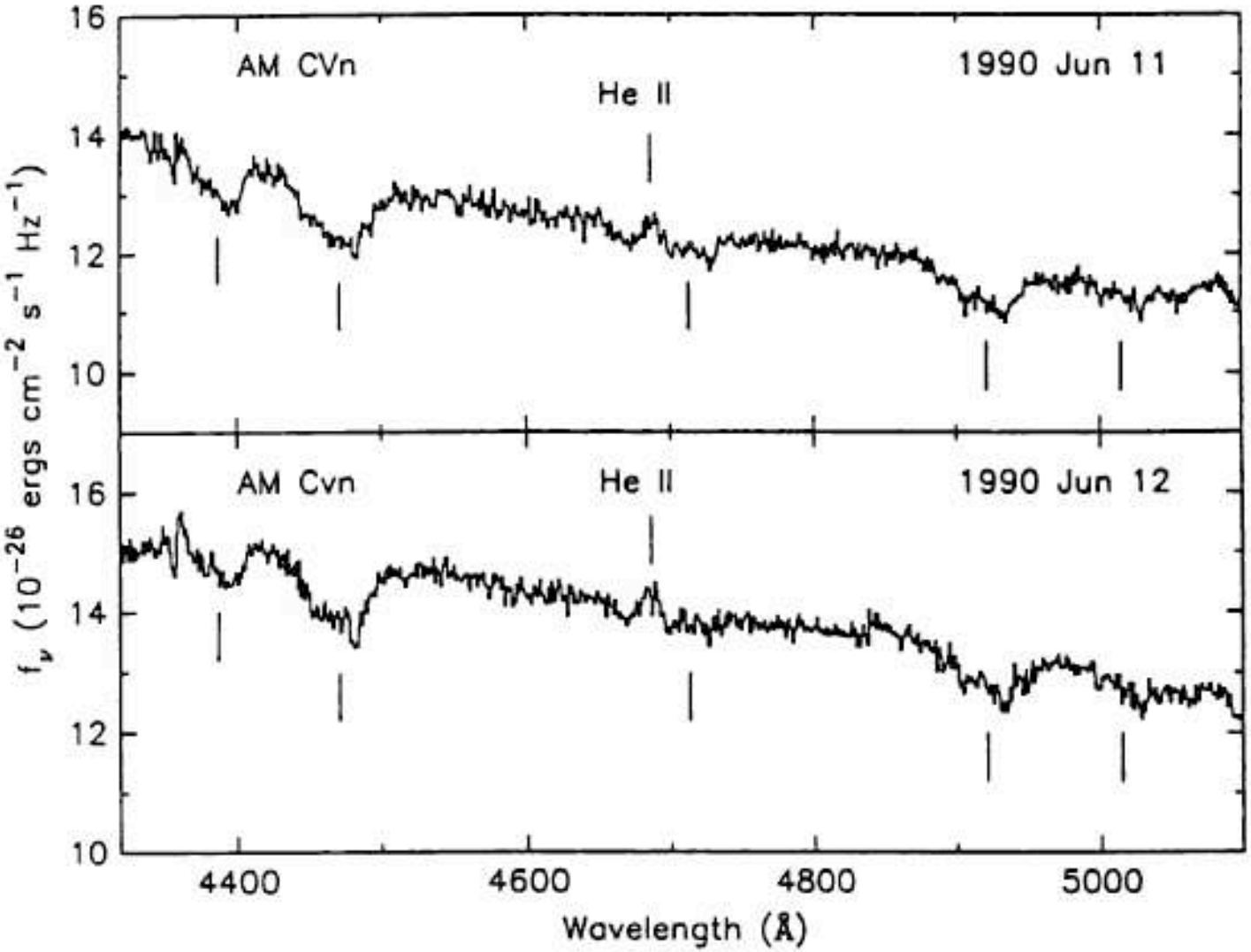


Fig. 7. Optical spectra of AM CVn and CR Boo. From Patterson *et al.* (1992).

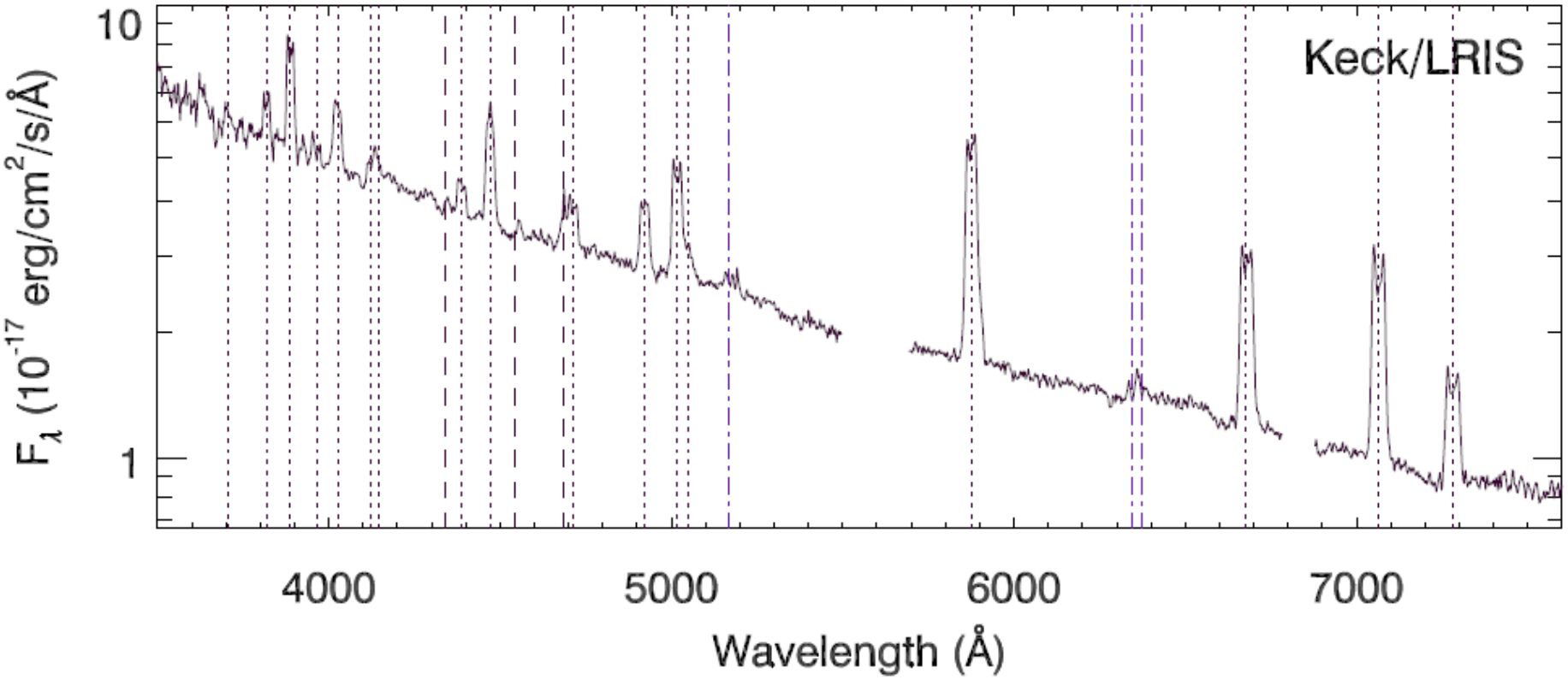


FIG. 6.— Average Keck-I/LRIS spectrum of SDSS J0902. Dotted and dashed lines mark the He I and He II emission features, respectively. The locations of Fe II ($\lambda$5169) and Si II ($\lambda$6347, 6371) in emission are indicated by the dash-dotted lines.

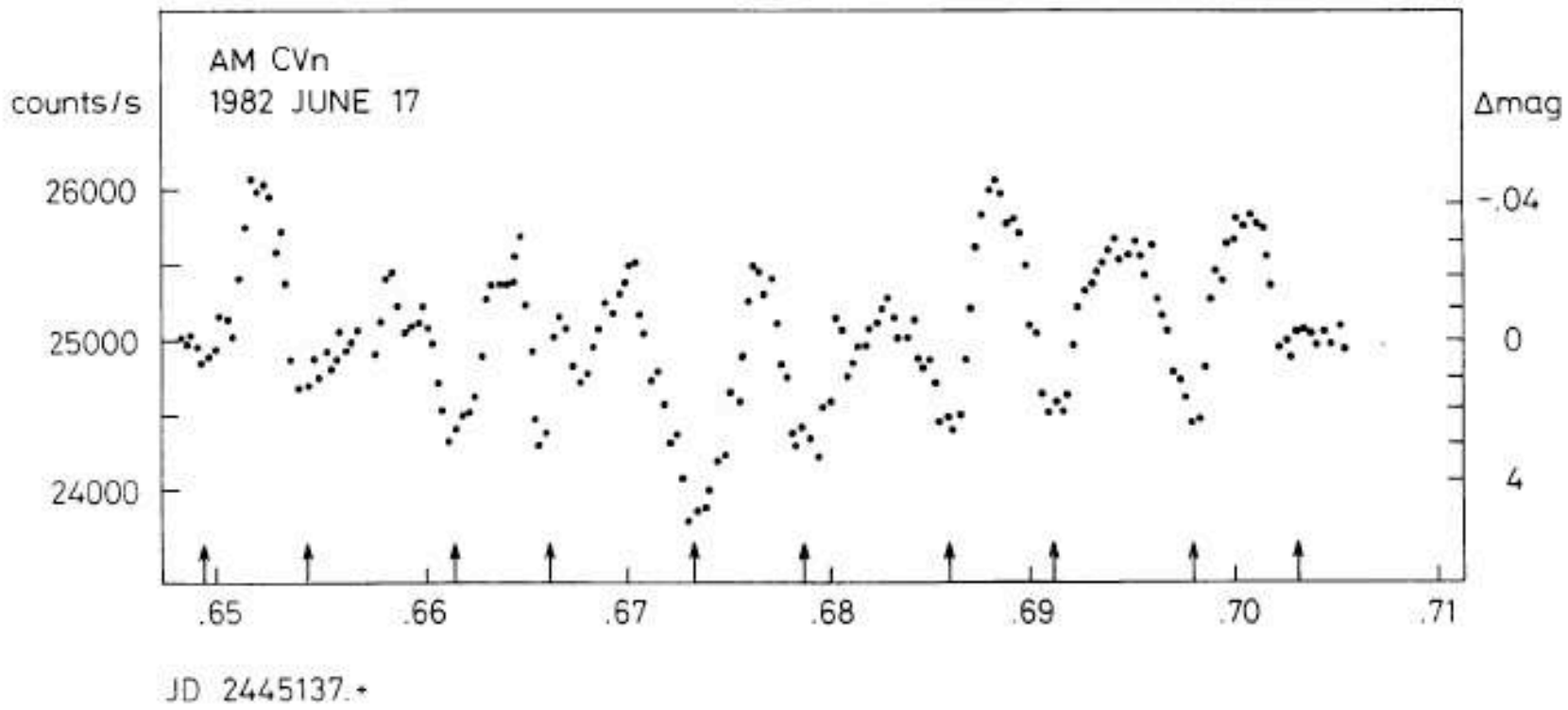
AM CVn
1982 JUNE 17
counts/s
26000
25000
24000
Δmag
-.04
0
4
.65
.66
.67
.68
.69
.70
.71
JD 2445137.+

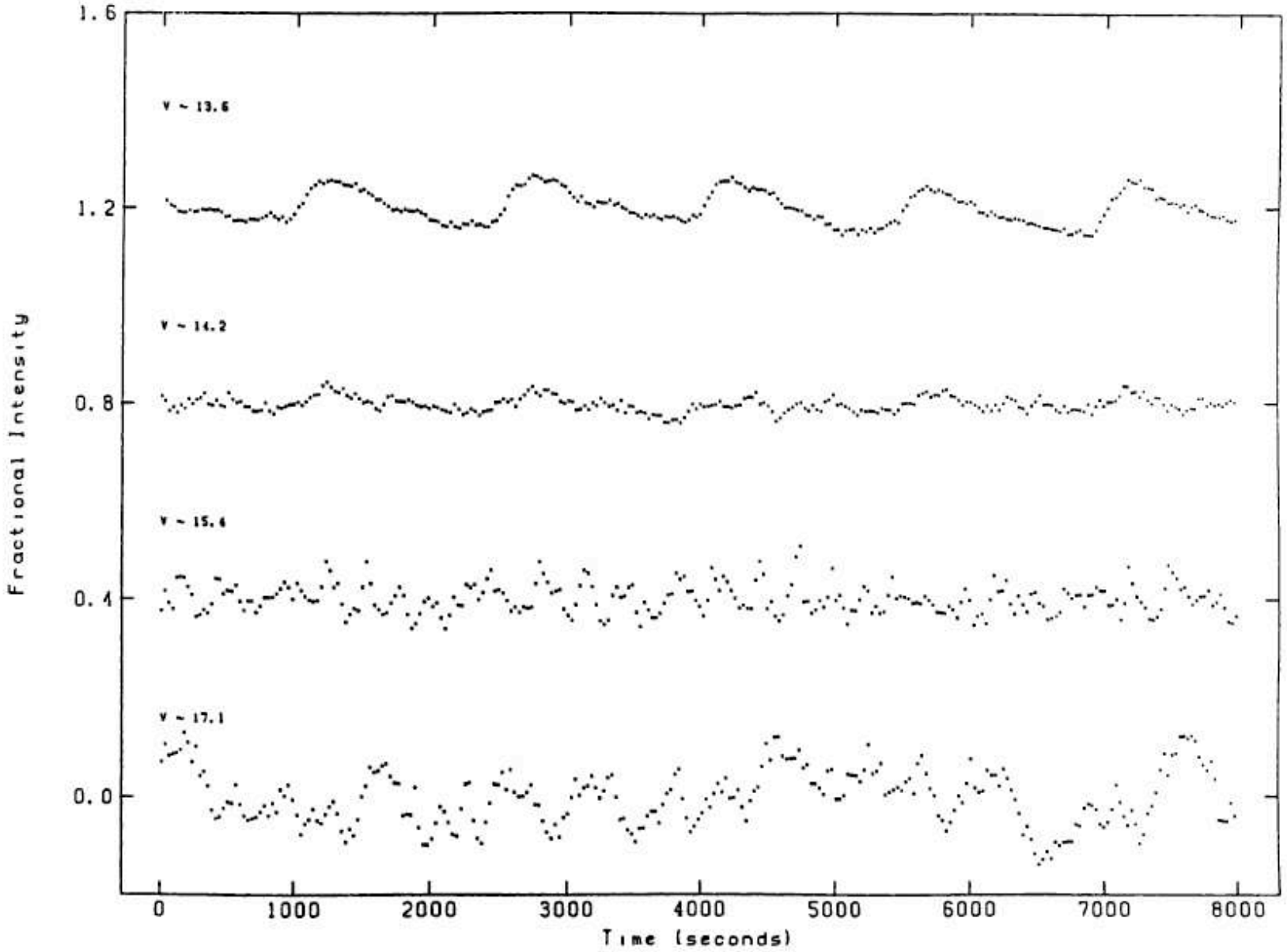


Fig. 6. Light curves of CR Boo at high, low and two intermediate states. From Wood *et al.* (1987).

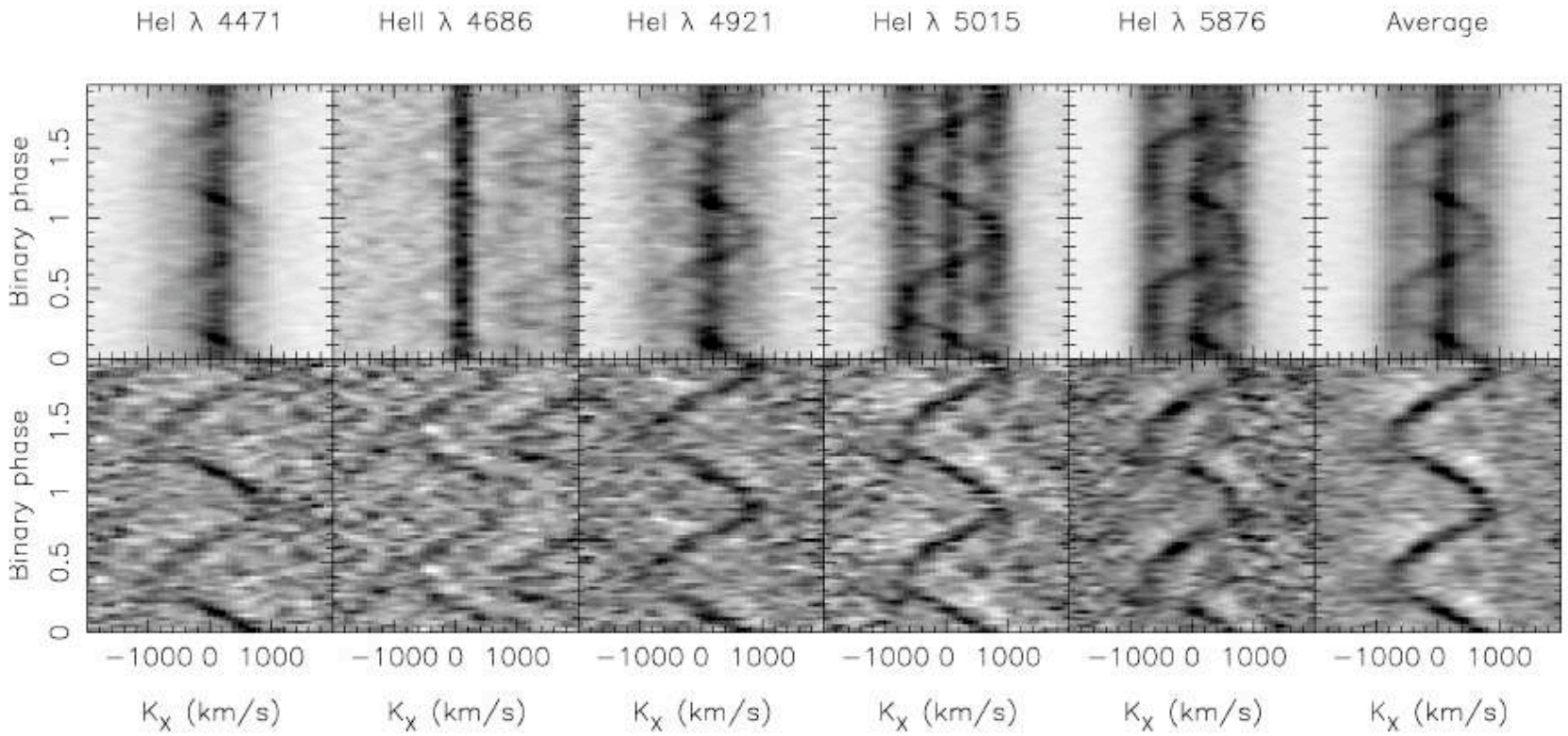


**Figure 5.** Trailed spectra (top row) and average-subtracted trailed spectra of the strongest He I and He II features. The right-most panels show the averages of these spectral lines.

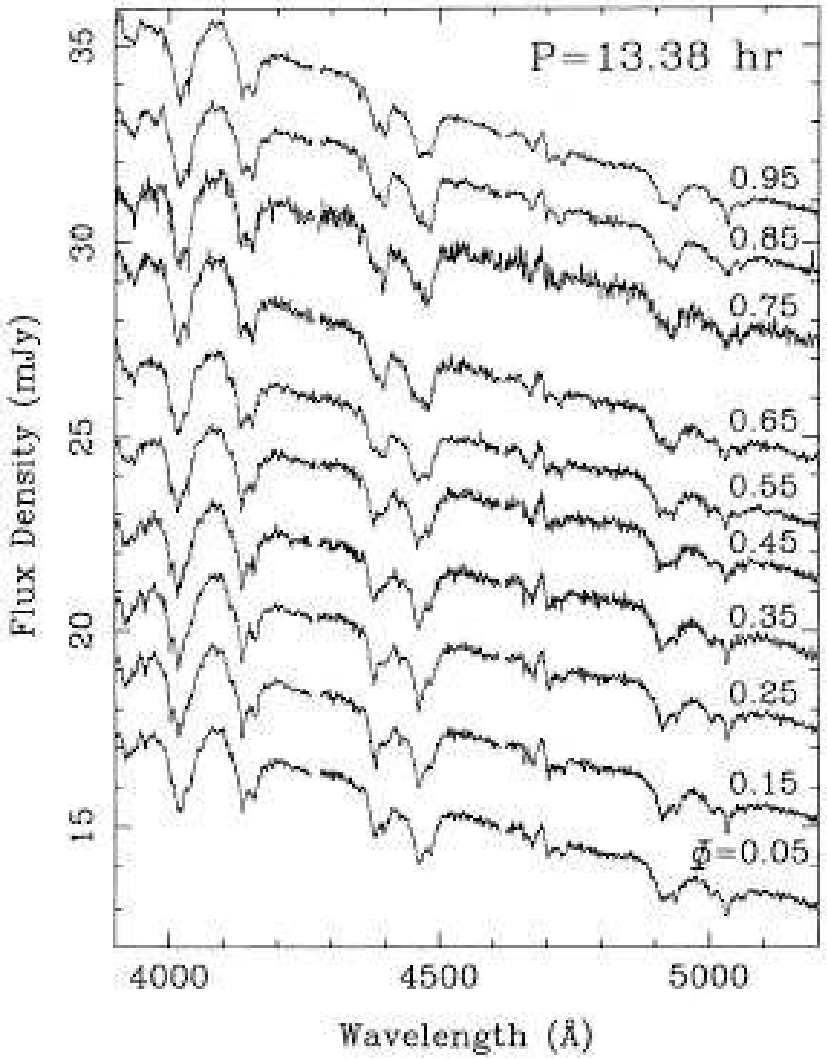
P=13.38 hr
0.95
0.85
0.75
0.65
0.55
0.45
0.35
0.25
0.15
$\bar{\phi}$=0.05
Flux Density (mJy)
15
20
25
30
35
4000
4500
5000
Wavelength (Å)

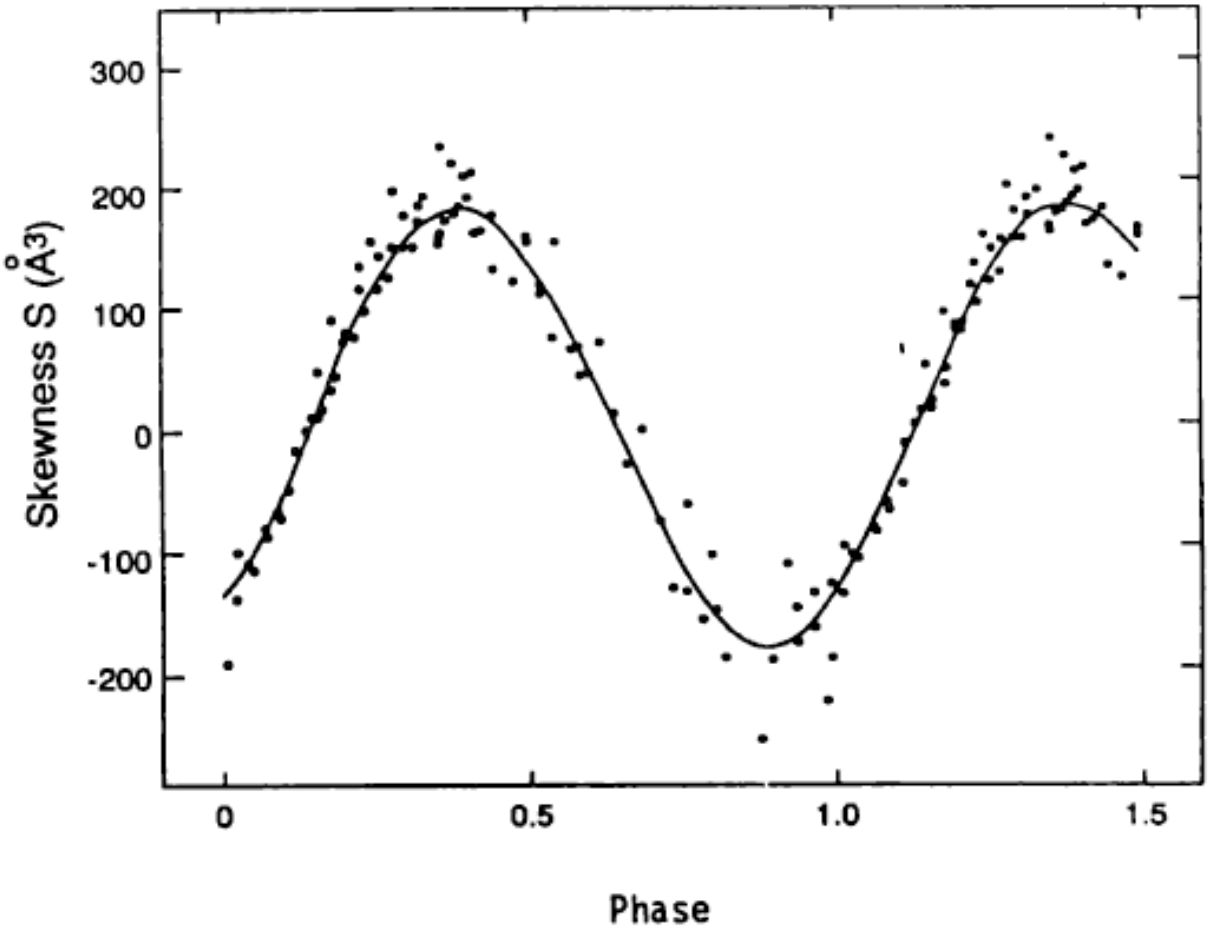


Fig. 8. Periodicity in skewness of absorption line profiles in AM CVn. From Patterson *et al.* (1993).

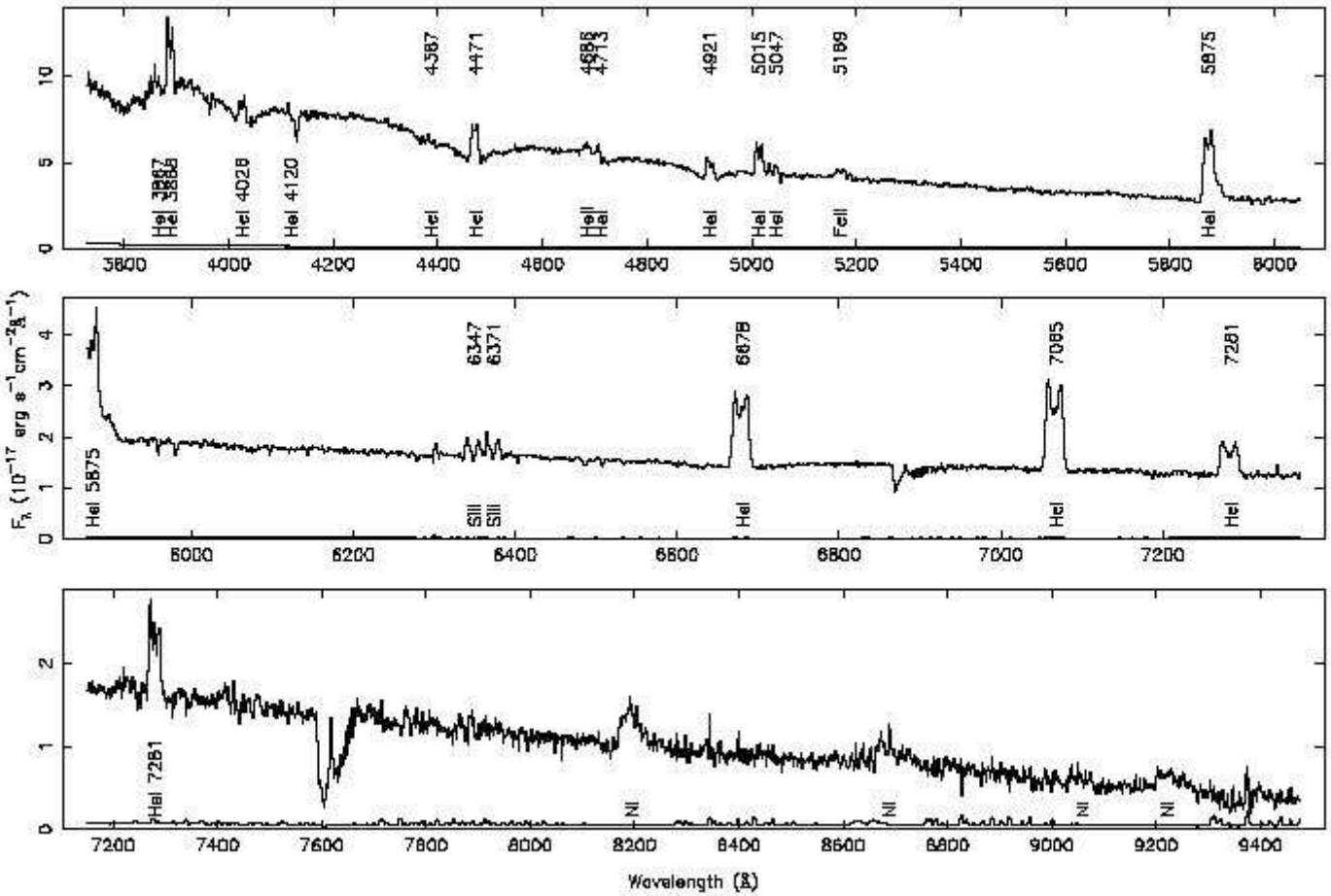
HeI 3867
HeI 3888
HeI 4026
HeI 4120
HeI
HeI
HeII
HeII
HeI
HeI
HeI
FeII
HeI
4387
4471
4686
4713
4921
5015
5047
5189
5875
HeI 5875
SiII
SiII
HeI
HeI
HeI
6347
6371
6678
7065
7281
HeI 7281
NI
NI
NI
NI
$F_\lambda$ ($10^{-17}$ erg s$^{-1}$cm$^{-2}$Å$^{-1}$)
Wavelength (Å)

Table 1: The AM CVn Stars

| Star | $P_{orb}(s)$ | $P_{sh}(s)$ | $P_{beat}(d)$ | $m_v$ | Refs |
|---|---|---|---|---|---|
| RXJ0806 | 321.25 | | | 21.1 | 1,2 |
| V407 Vul (RX J1914+24) | 569 | | | 19.9 | 3 |
| ES Cet (KUV 01584-0939) | 620 | | | 16.9 | 4,5 |
| AM CVn | 1028.7 | 1054 | 0.50 | 14.1- 14.2 = 0.1 | 6,7 |
| HP Lib (EC 15330) | 1102.7 | 1119 | 0.88 | 13.6 | 8 |
| CR Boo | 1471.3 | 1487 | 1.61 | 13.0 -18.0 = 5.0 | 9,10,11,12 |
| KL Dra | 1500 | 1530 | 0.89 | 16.8 - 20 = 3.2 | 13 |
| V803 Cen (AE1) | 1612.0 | 1618.3 | 4.79 | 13.2 -17.4 = 3.8 | 14,15,16 |
| SDSS 0926 | 1698 | | | 18.8 - > 1.0 | 25 |
| CP Eri (PHL 1475) | 1701.2 | 1715.9 | 2.29 | 16.5 - 19.7 = 3.2 | 17 |
| Hya (SN2003aw) | | 2041.5 | | 16.5 - 20.3 = 3.8 | 18 |
| ROTSE (2QZ J1427) | 2194 | | | 15.1 - 20.2 = 5.1 | 19 |
| Vir (SDSS 1240) | 2237.5 | 2253.2 | | <18.2 -19.7 > 1.5 | 20 |
| GP Com | 2794 | | | 15.7 - 16.0 = 0.3 | 21,22 |
| V396 Hya (CE-315) | 3906 | | | 17.6 | 23,24 |
| SDSS 0129 | | | | 19.7 | 25 |
| SDSS 1411 | | | | 19.4 | 25 |
| SDSS 1552 | | | | 20.2 | 25 |

References 1. Israel et al (2002); 2. Ramsay, Hakala & Cropper (2002); 3. Cropper et al (1998); 4. Warner & Woudt (2002); 5. Espaillat et al 2005; 6. Skillman et al (1999); 7. Solheim et al (1998); 8. Patterson et al (2002); 9. Kato et al (2000a); 10. Kato et al (2001b); 11. Patterson et al (1997); 12. Provencal et al (1997); 13. Wood et al (2002); 14. Kato et al (2000a,b); 15. Kato et al (2001a); 16. Patterson et al (2000); 17. Abbott et al (1992); 18. Woudt & Warner (2003); 19. Woudt, Warner & Rycoff (2005); 20. Roelofs et al (2004); 22. Woudt & Warner (2005); 21. Nather, Robinson & Stover 1981; 22. Morales-Rueda et (2003); 23. Ruiz et al (2001); 24. Woudt & Warner (2002); 25. Anderson et al 2005.

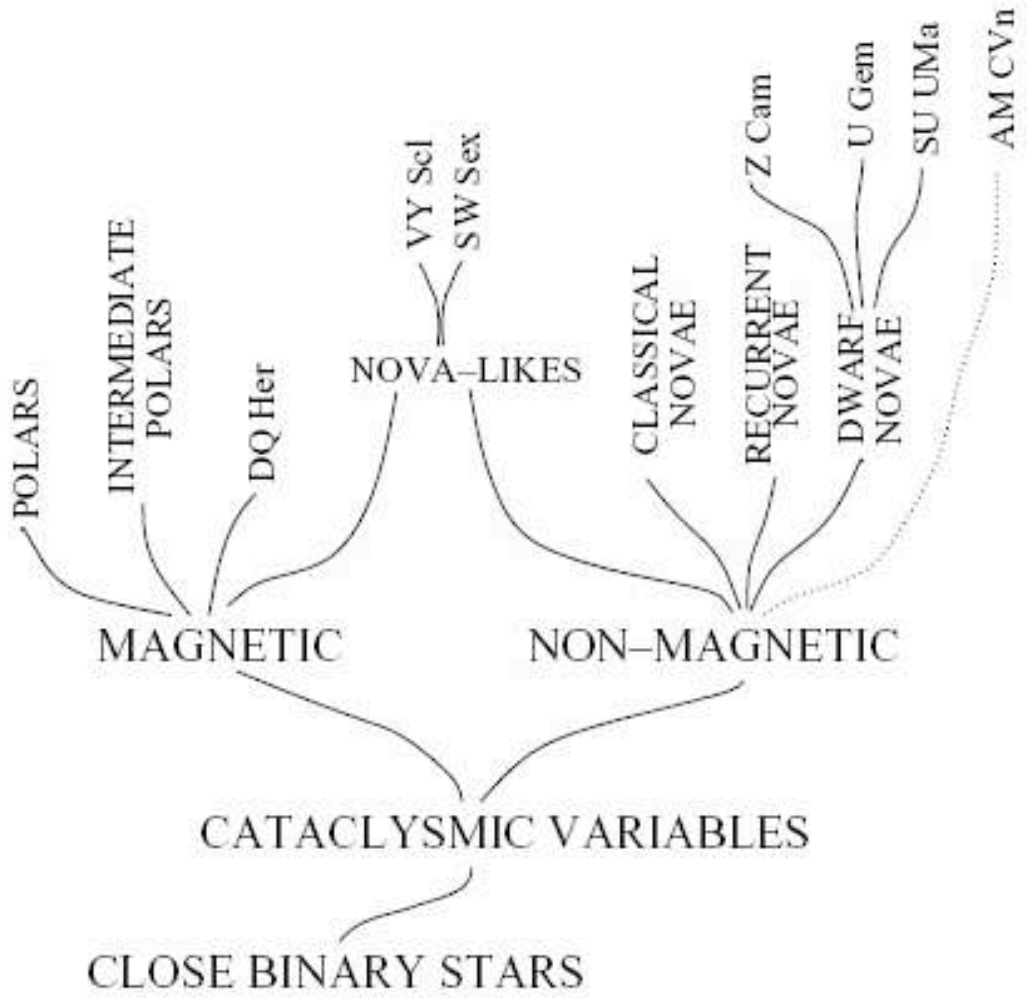


**Figure 1.** Partial hierarchy of close binary systems from general (base) to more specific (top). Mostly hydrogen systems are shown with a solid line and mainly helium systems are shown with a dotted line.

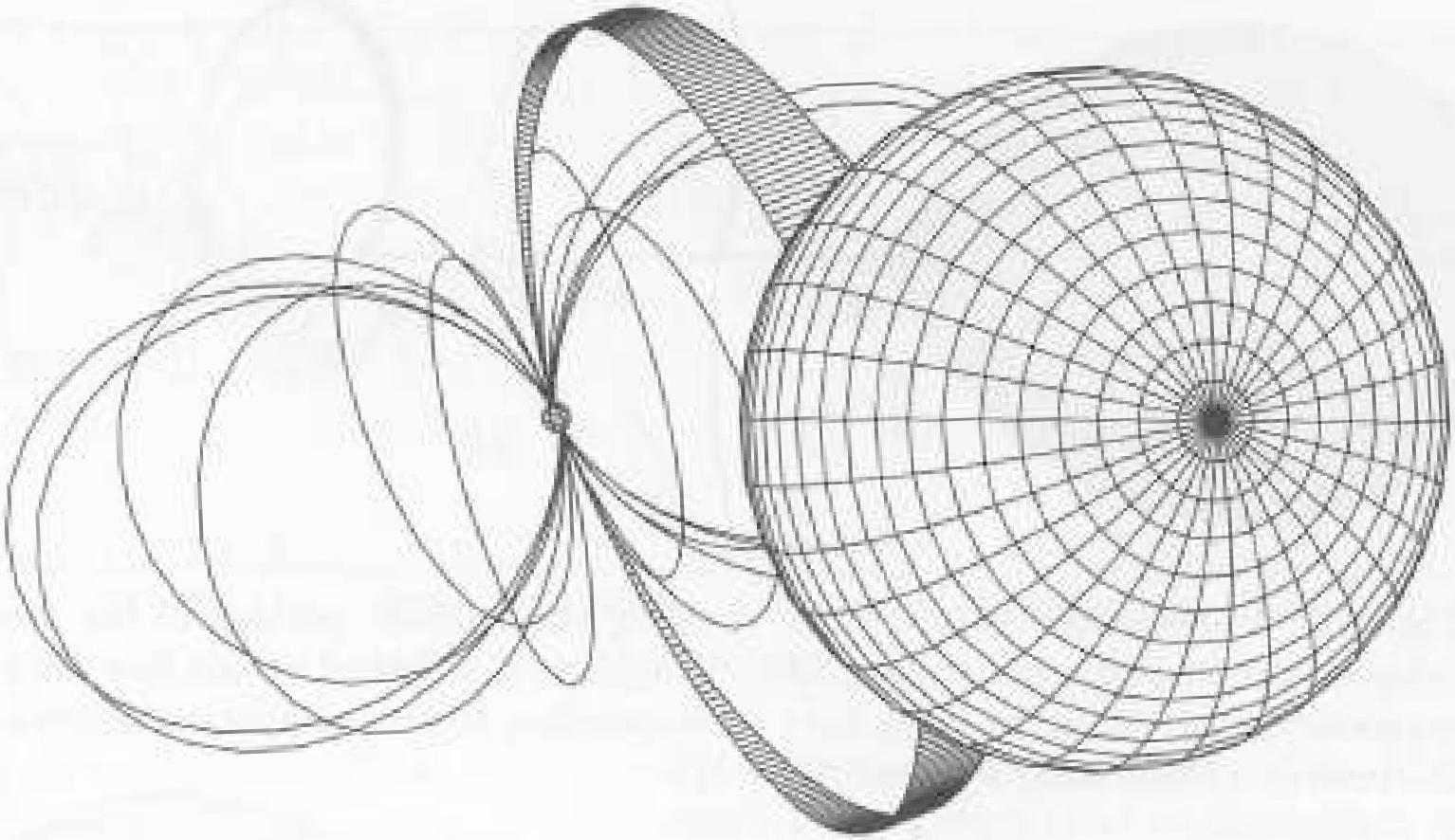

Fig. 8.1: In AR UMa the accretion stream emerges from the $L_1$ point, splits into two, and follows field lines onto the magnetic poles of the white dwarf. The dipole pattern of the field lines is shown. (Illustration by Gary Schmidt.[1])

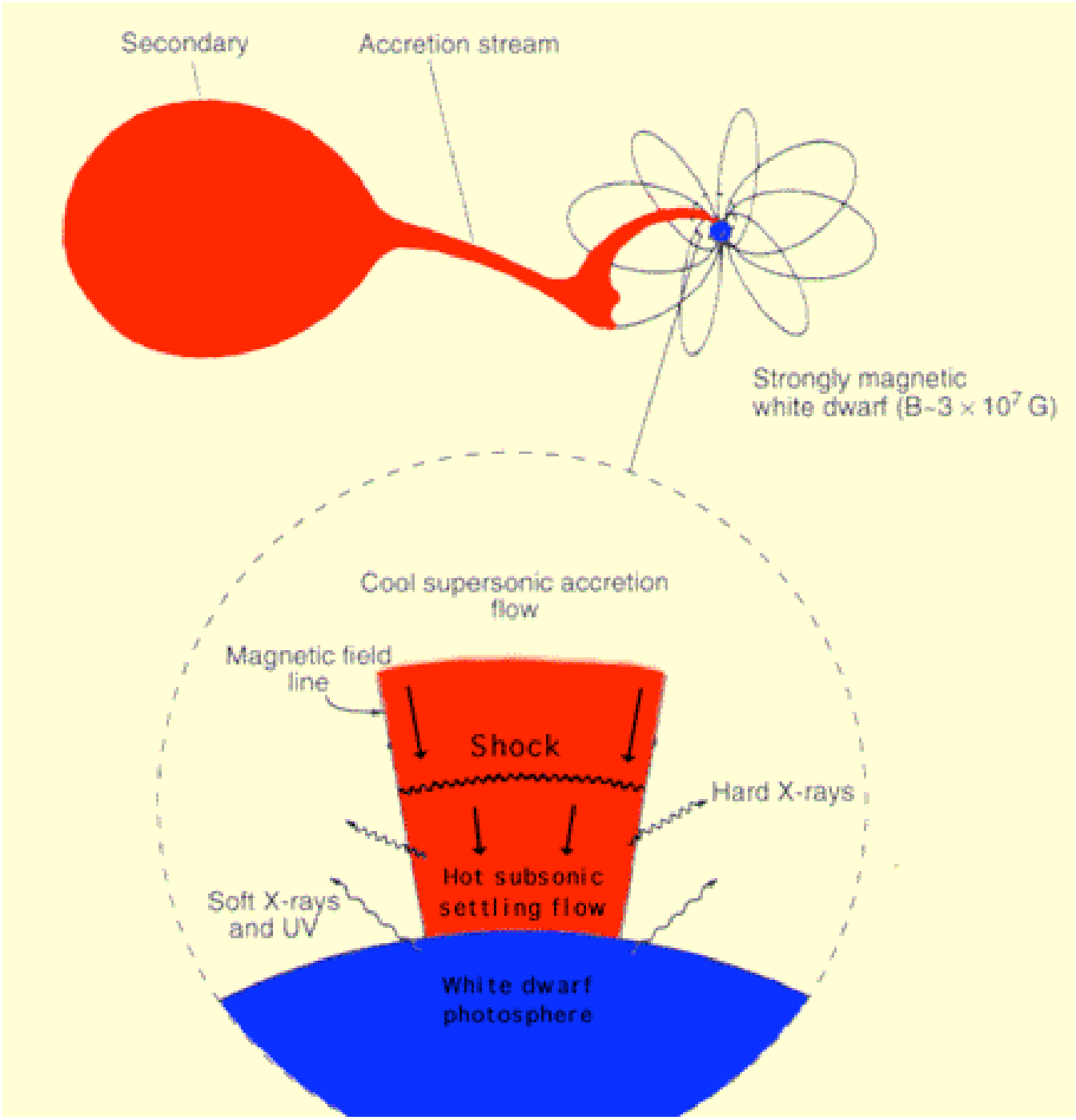
Secondary
Accretion stream
Strongly magnetic
white dwarf (B~3 × 10^7 G)
Cool supersonic accretion
flow
Magnetic field
line
Shock
Hard X-rays
Hot subsonic
settling flow
Soft X-rays
and UV
White dwarf
photosphere

# Accretion funnels replace disks in magnetic CVs (Polars)

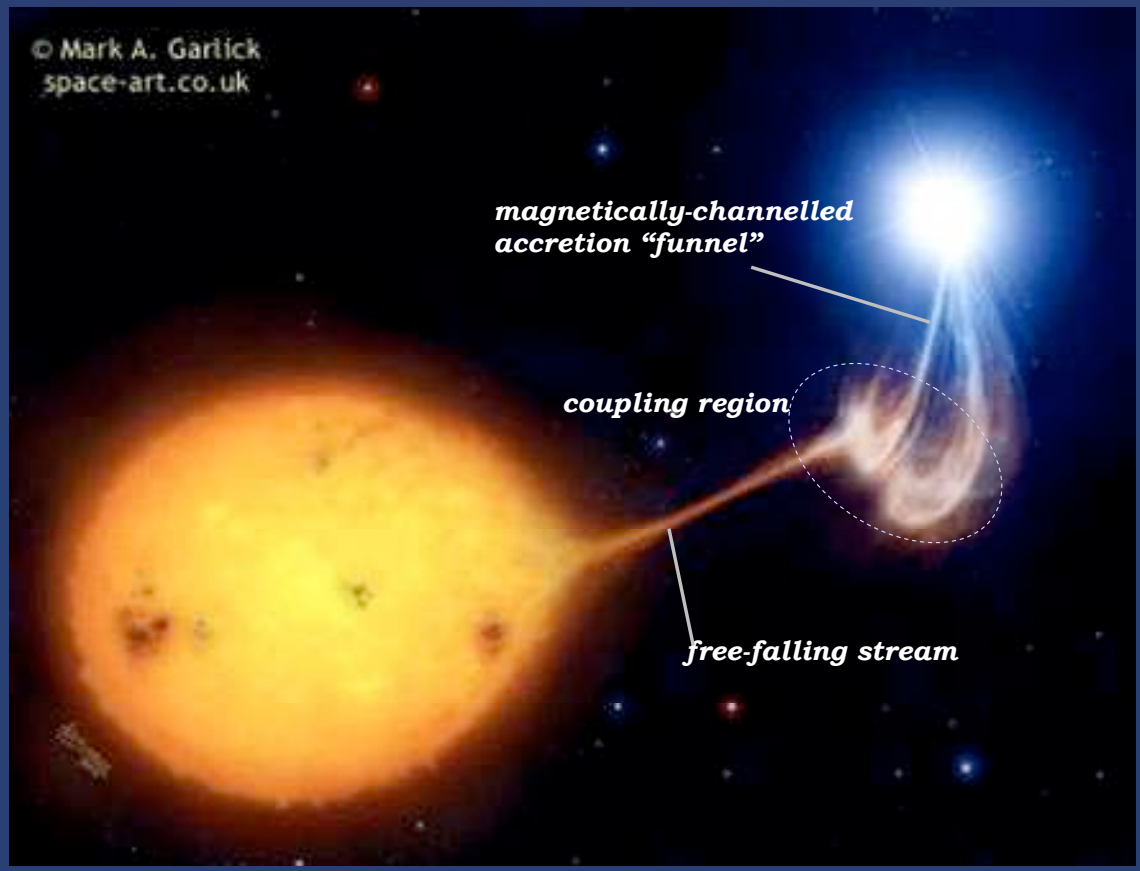

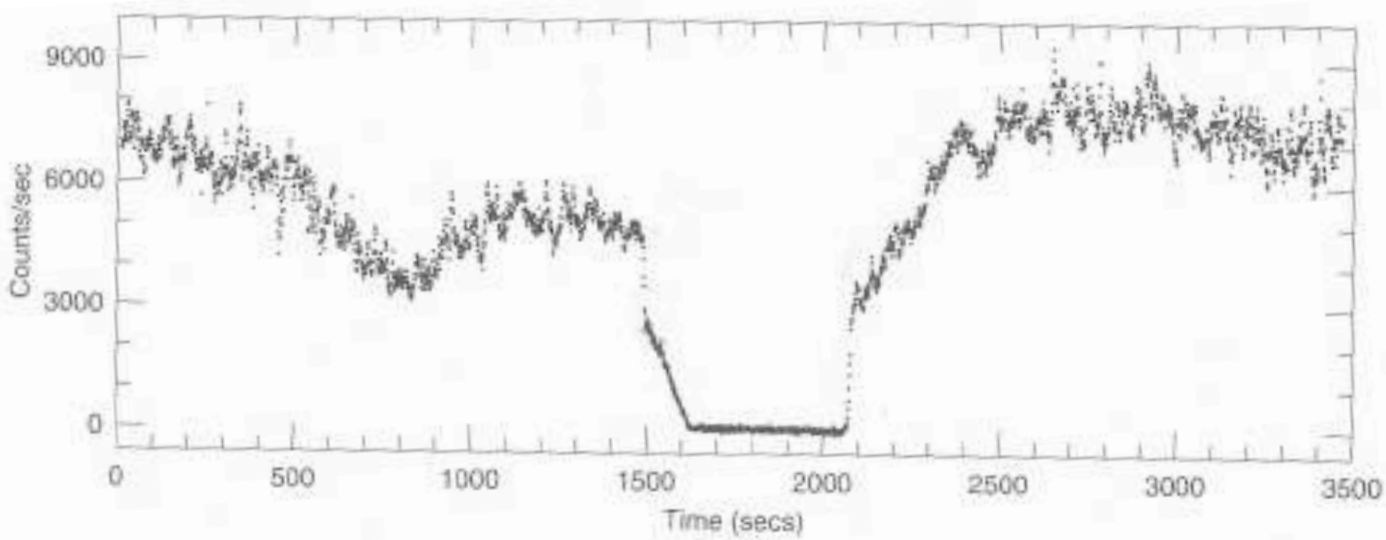


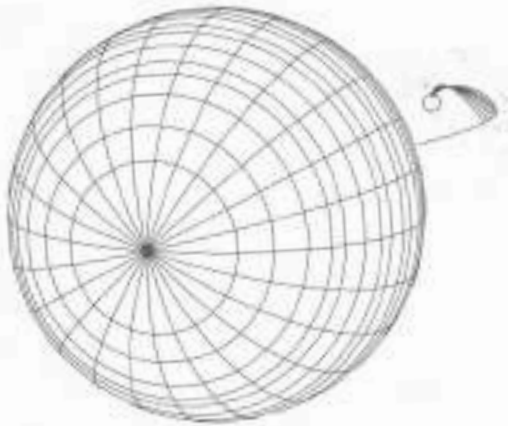

Fig. 8.3: An optical lightcurve of the AM Her star HU Aqr (*above*) and an illustration of the system approaching eclipse (*left*), corresponding to 1300 sec in the above plot.[4] At 1490 sec the tiny accretion spot is eclipsed, and the light drops dramatically. The bright stream enters eclipse over the next 130 sec. At the end of the eclipse the accretion spot suddenly emerges from behind the red dwarf (2075 sec), followed by the stream (2075–2300 sec). Earlier, at around 800 sec, the stream had been in front of the accretion spot, absorbing some of its light and causing a dip in the lightcurve.

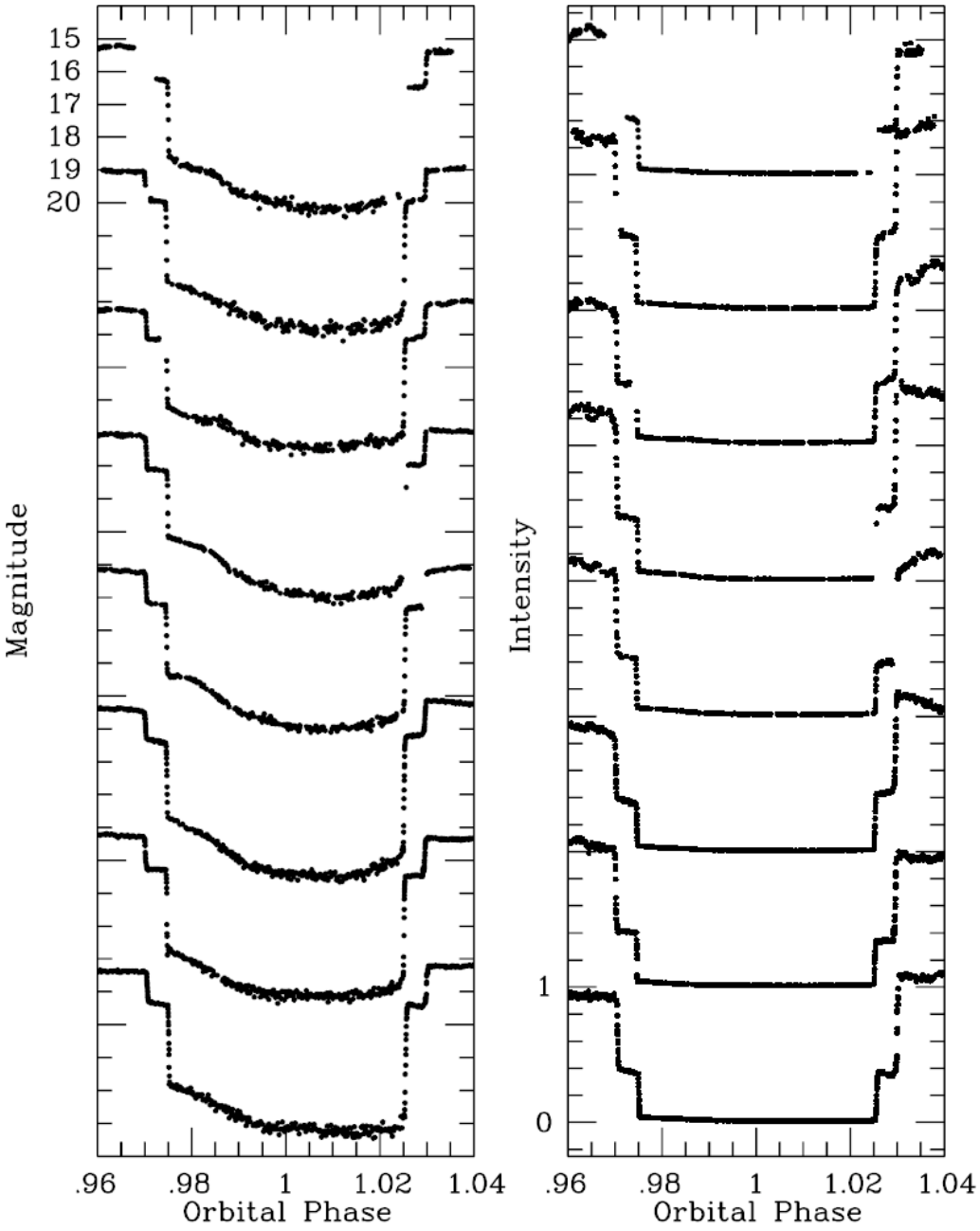
15
16
17
18
19
20
Magnitude
.96
.98
1
1.02
1.04
Orbital Phase
Intensity
1
0
.96
.98
1
1.02
1.04
Orbital Phase

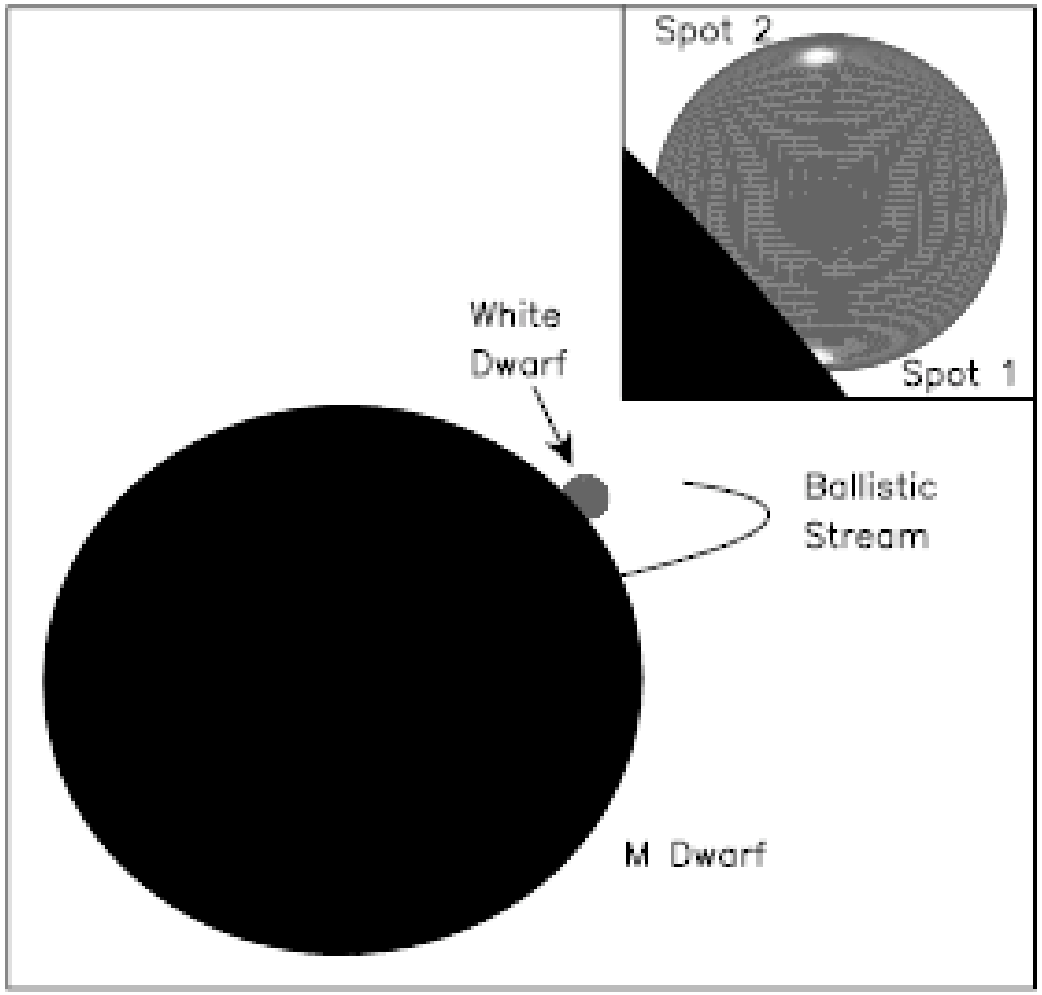
Spot 2
White
Dwarf
Spot 1
Ballistic
Stream
M Dwarf

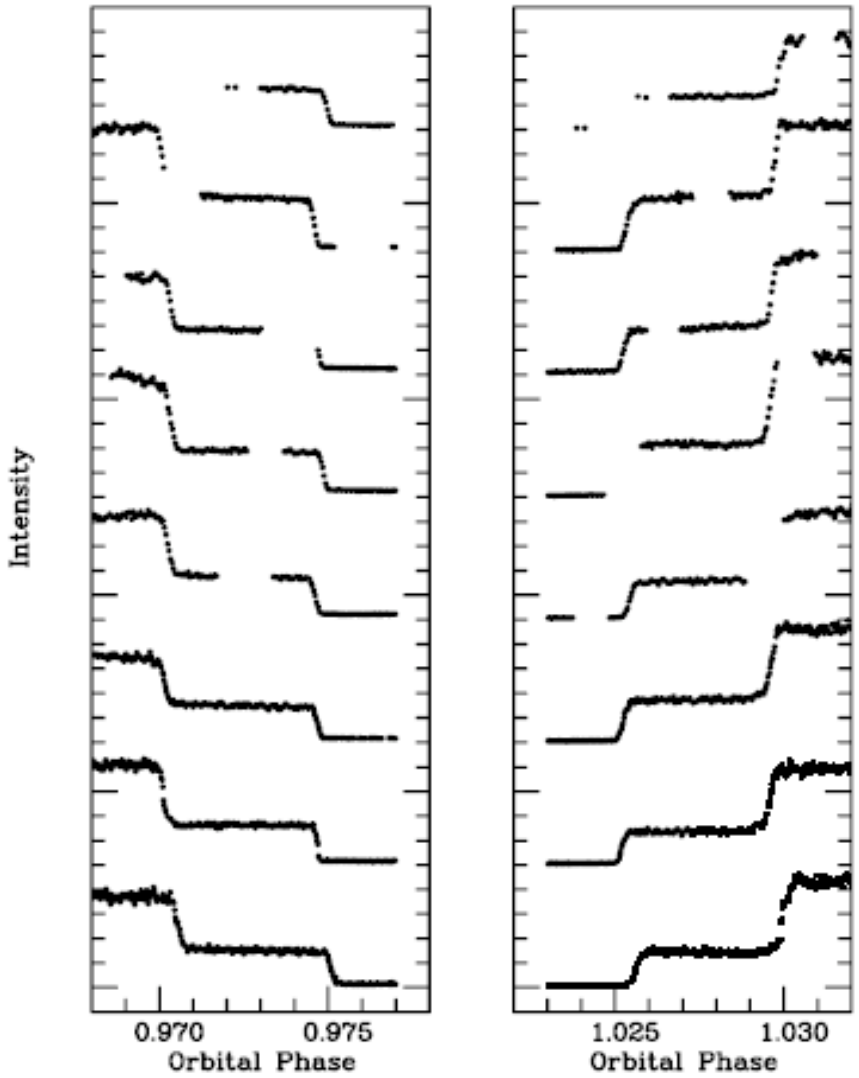


**Figure 3.** Ingress and egress detail. The ordering of the individual runs is as in Figs 1 and 2. The horizontal axis is orbital phase using the ephemeris of equation (1). Individual carets (0.001 phase) correspond to ~5.2 s. The vertical axis is relative intensity as for Fig. 1. Its zero-point is indicated by the lowest caret on the vertical axis. Individual runs have been offset from their neighbours by five carets on the vertical axis.

**Doppler tomogram of HU Aquarii**

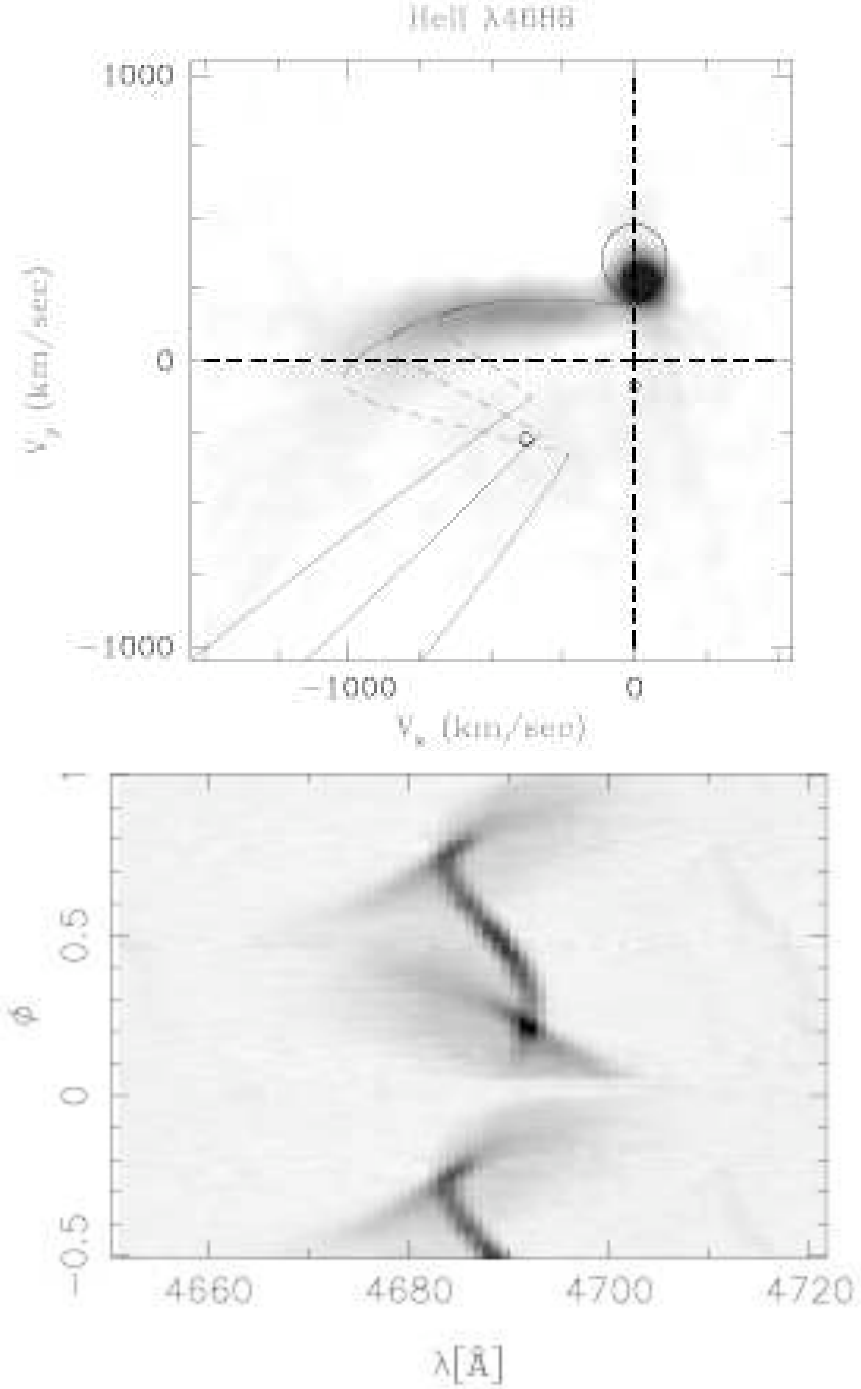

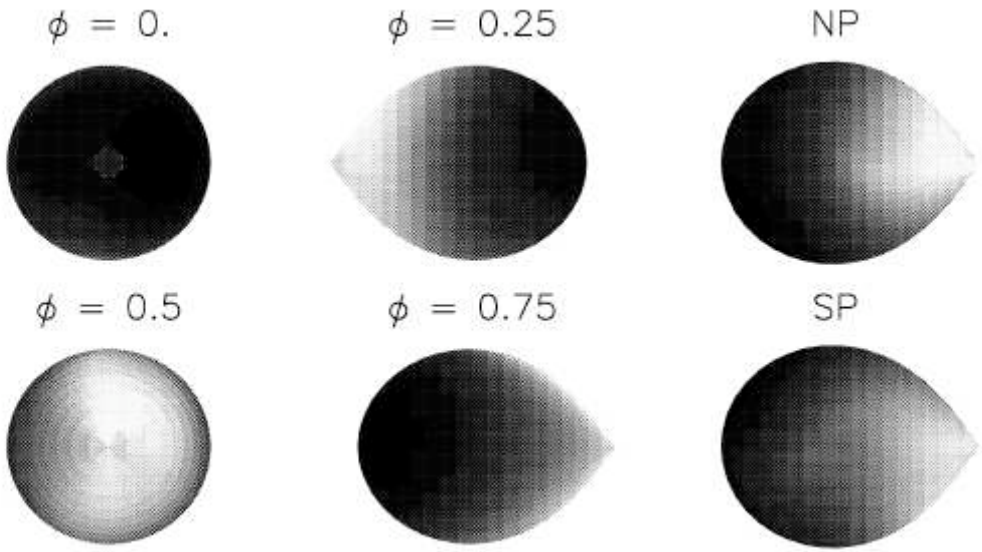


**Brightness distribution on the secondary of HU Aqr**

# Polarization of cyclotron emission

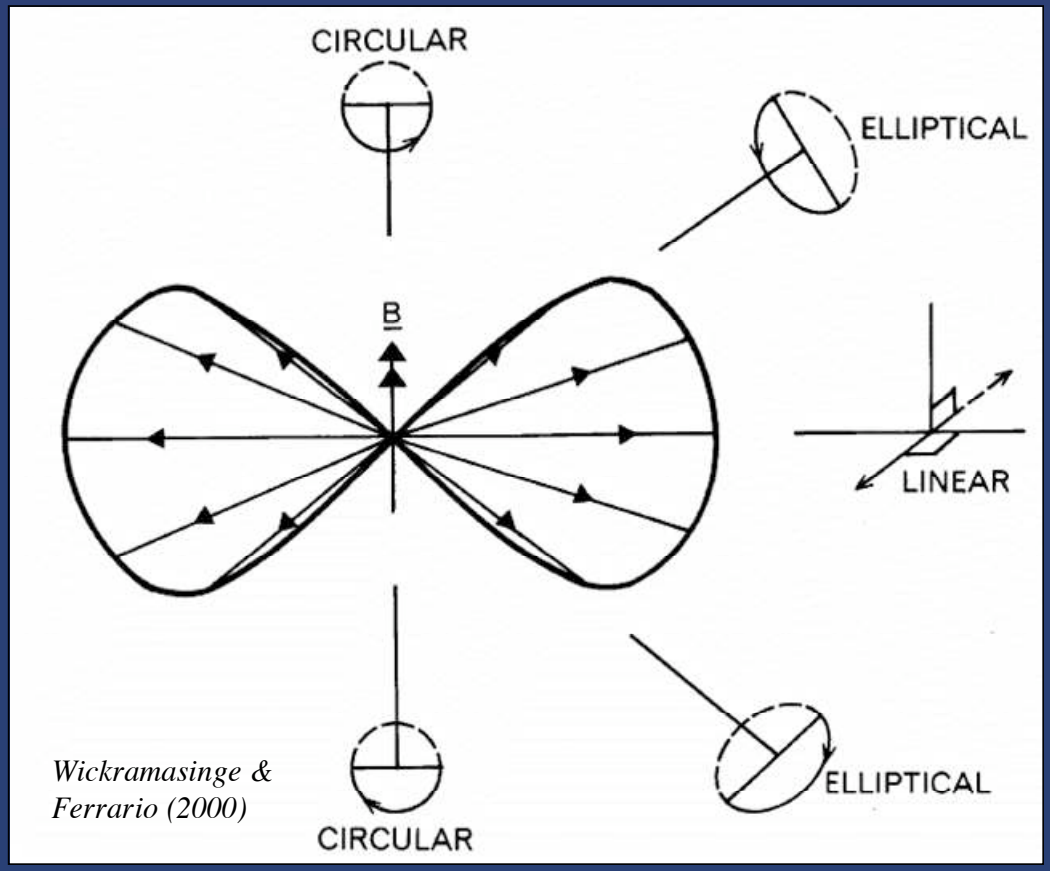


*Wickramasinge & Ferrario (2000)*

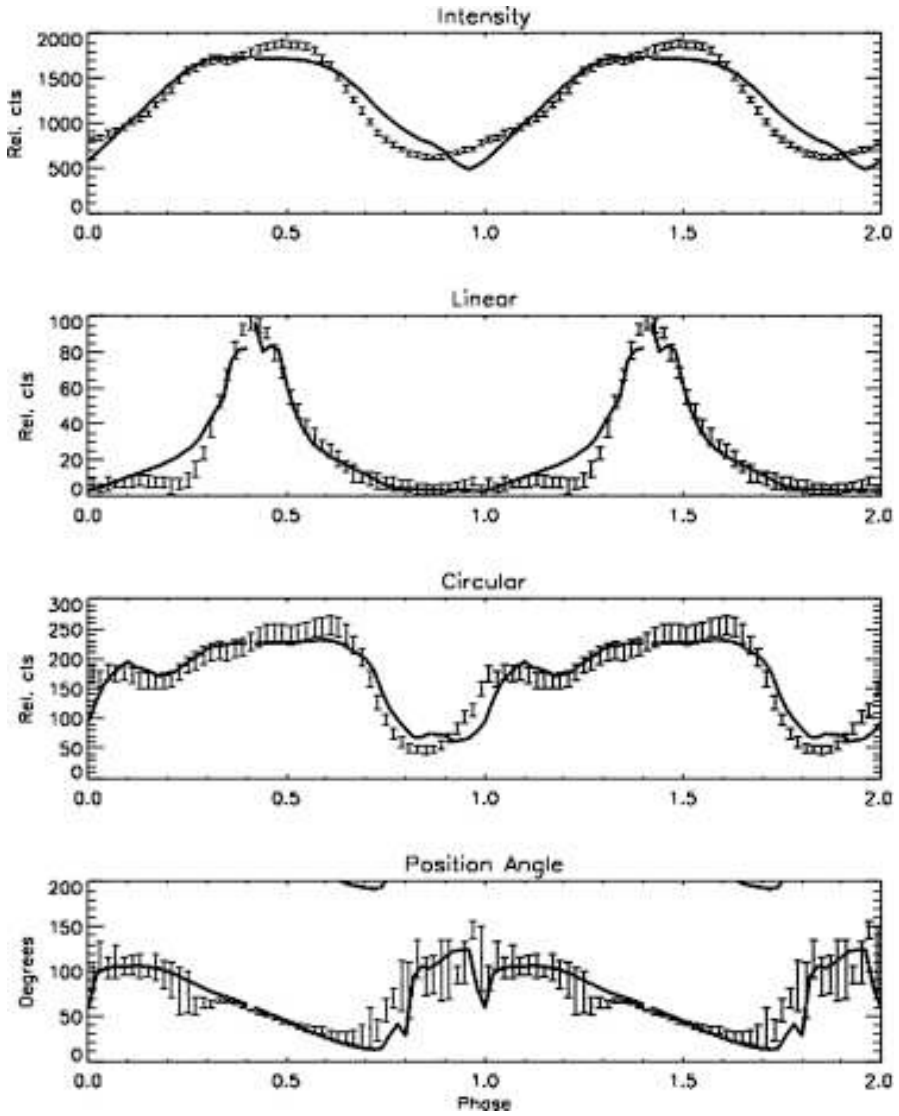


Photo-polarimetric observations of the polar V834 Cen (from Potter et al., 2004). Solid curves are a model fit (see text).

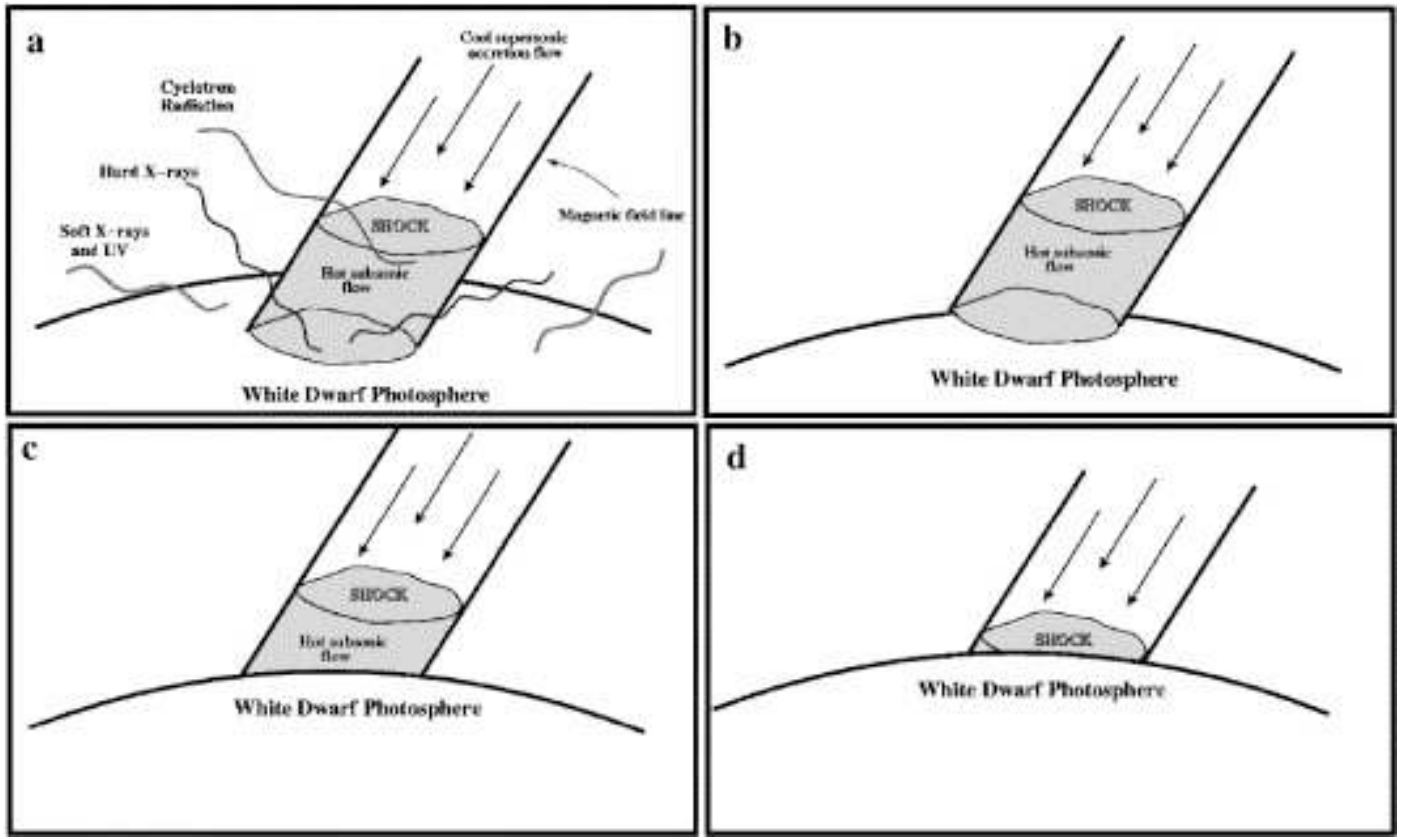


Fig. 6. Diagram showing the accretion column/shock disappearing (a)–(d) over the limb of the white dwarf

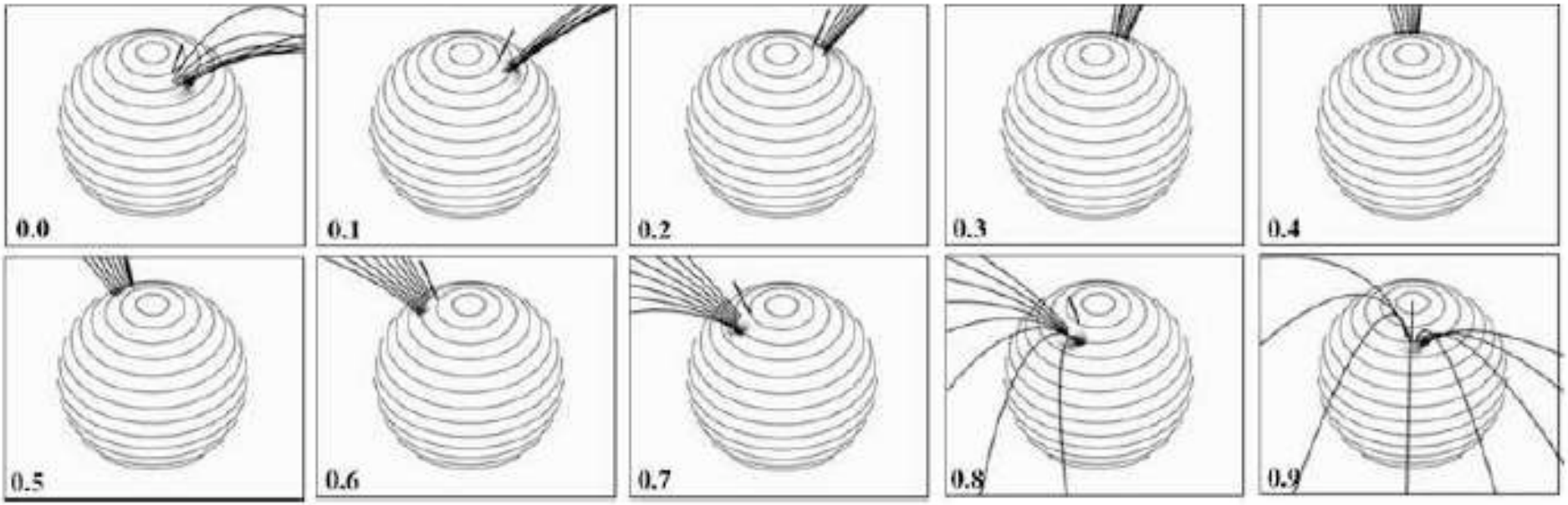


**Figure 2.** View from the Earth of the white dwarf in V834 Cen for a complete orbital rotation. The predicted cyclotron emission region is shown as the (small) grey-scale region. The magnetic pole is indicated by a short solid line at latitude 10 degrees from the spin pole. Latitudes are indicated every 10 degrees. Magnetic field lines (see Section 4.1) are shown as solid lines.

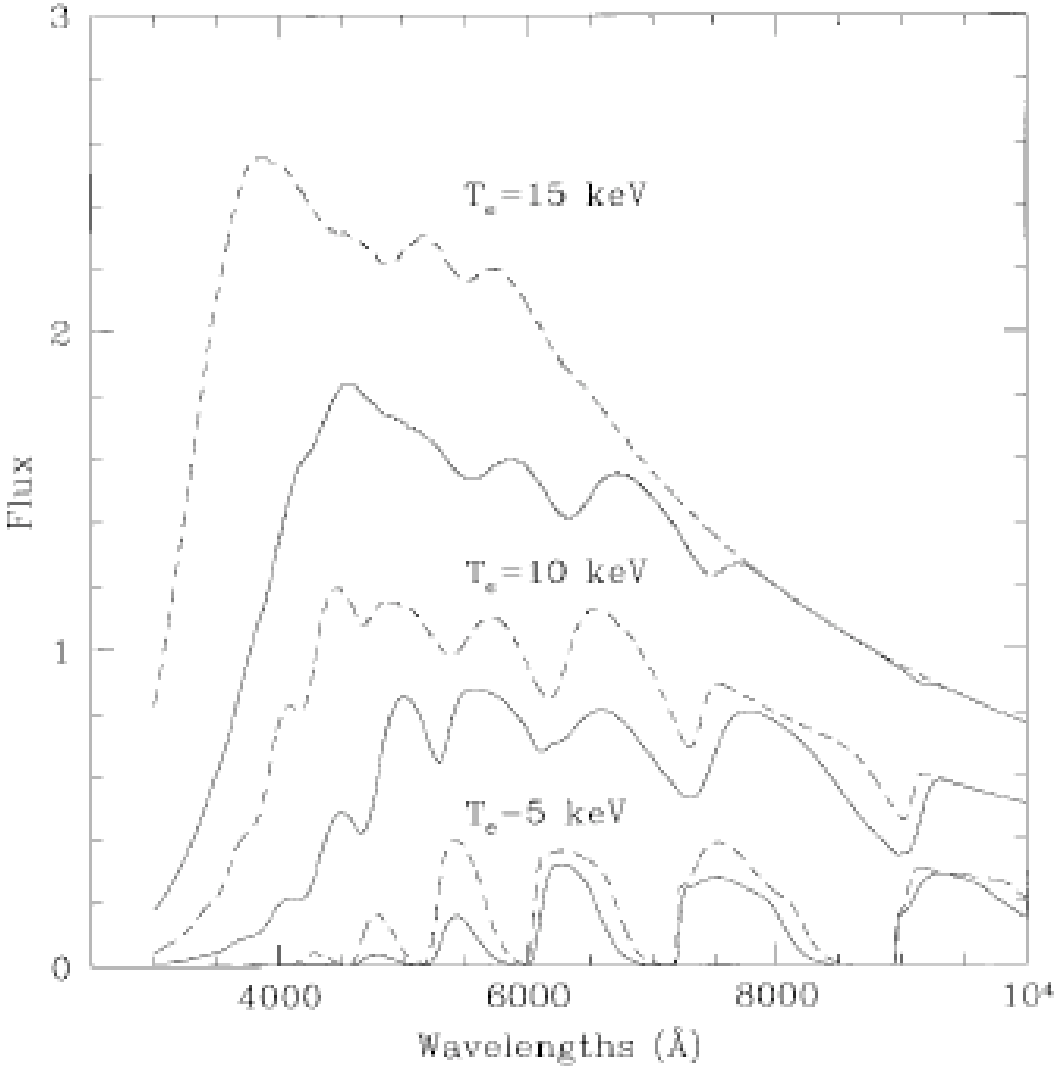


FIG. 32.—Theoretical cyclotron spectra ($I_\nu$) as a function of electron temperature $T_e$ for a viewing angle $\theta = 90°$. The solid and dashed curves are for optical depth parameter $\Lambda = 2 \times 10^5$ and $\Lambda = 10^6$, respectively. The magnetic field $B = 30$ MG.

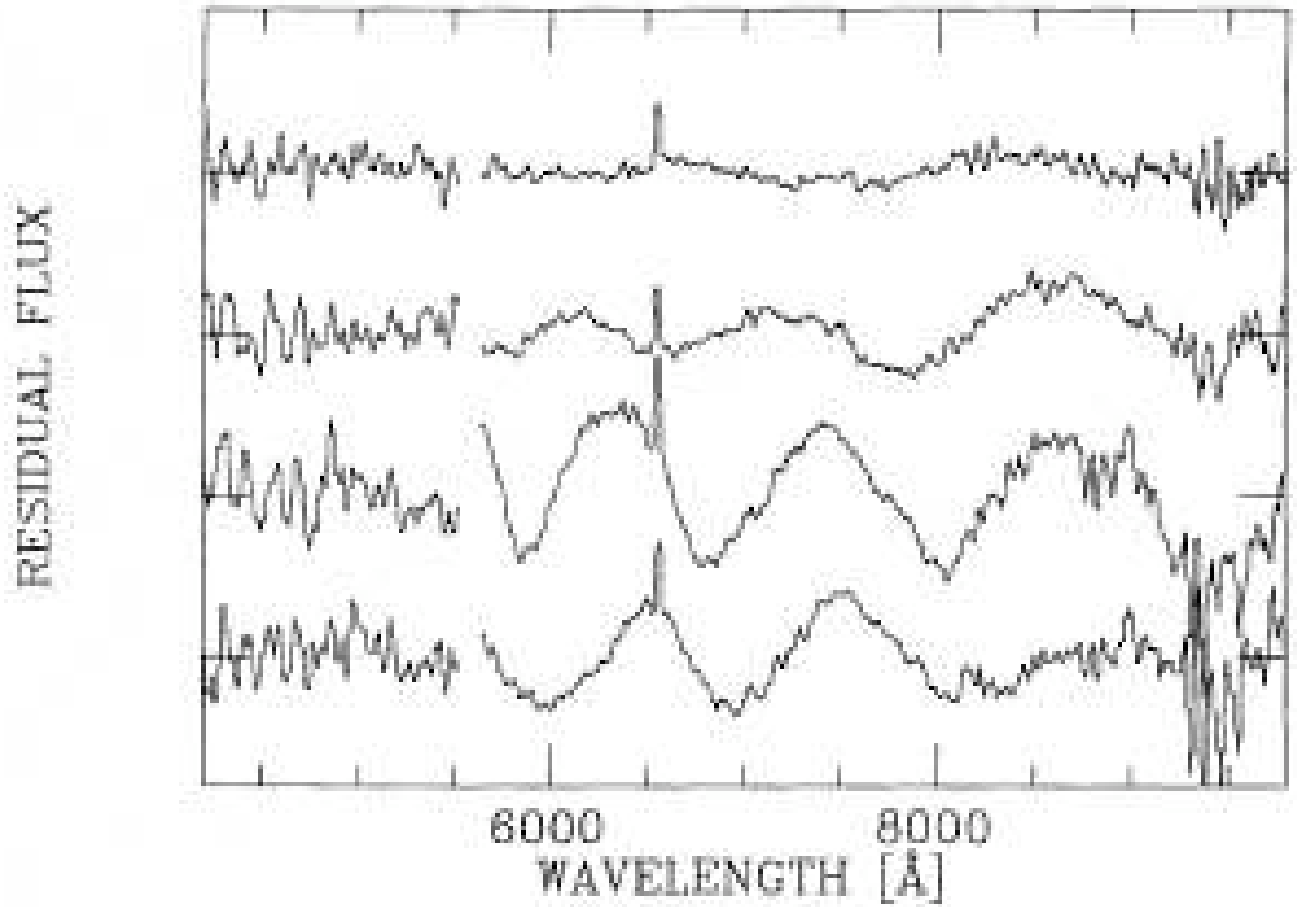


**Fig. 8.** Continuum-subtracted low-resolution spectra obtained in the 1991 low state. The spectra belong to spectral phases 0.41, 0.50, 0.58 and 0.67 from bottom to top, respectively

**MR Serpentis**

# MR Serpentis

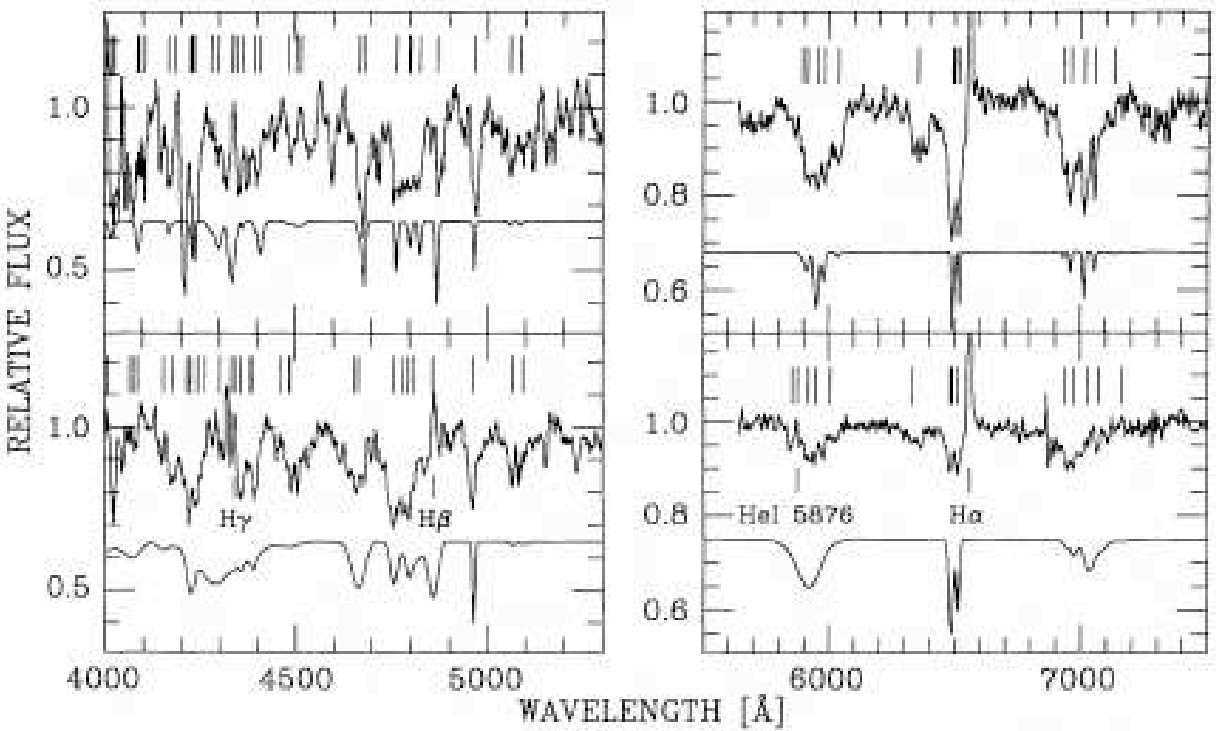


**Fig. 11.** Normalized spectra at phases 0.0 (upper panels) and 0.5 (lower panels) of the 1991 low state. Predicted positions of individual Zeeman lines of H$\alpha$, H$\beta$, and H$\gamma$ are marked by short vertical lines above the spectra. The field strengths used for calculation was 27.3 MG ($\phi_{sp} = 0.0$) and 28.5 MG ($\phi_{sp} = 0.5$), respectively. Below the observed spectra we show average absorption coefficients smeared assuming Gaussian field distributions with central field strengths as above and $\sigma_B = 0.3$ MG and 1.5 MG, respectively

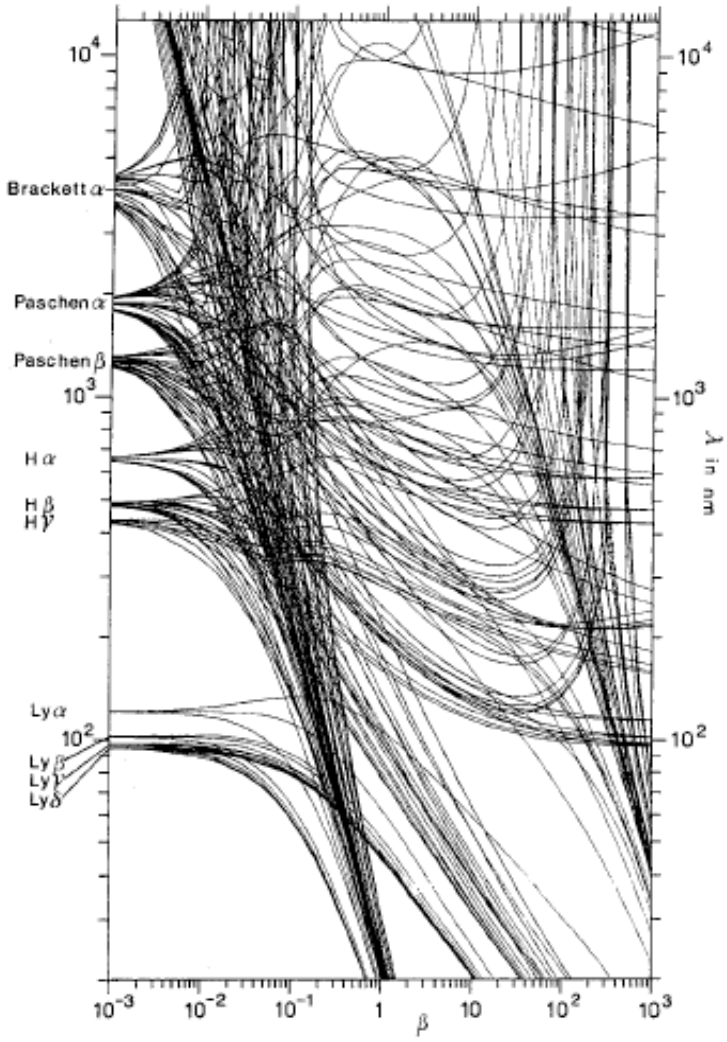


FIG. 2.—Calculations of the Zeeman splitting of hydrogen as a function of the magnetic field parameter $\beta = B/4.7 \times 10^9$ G from Wunner (1990). Copyright American Institute of Physics, reproduced with permission.

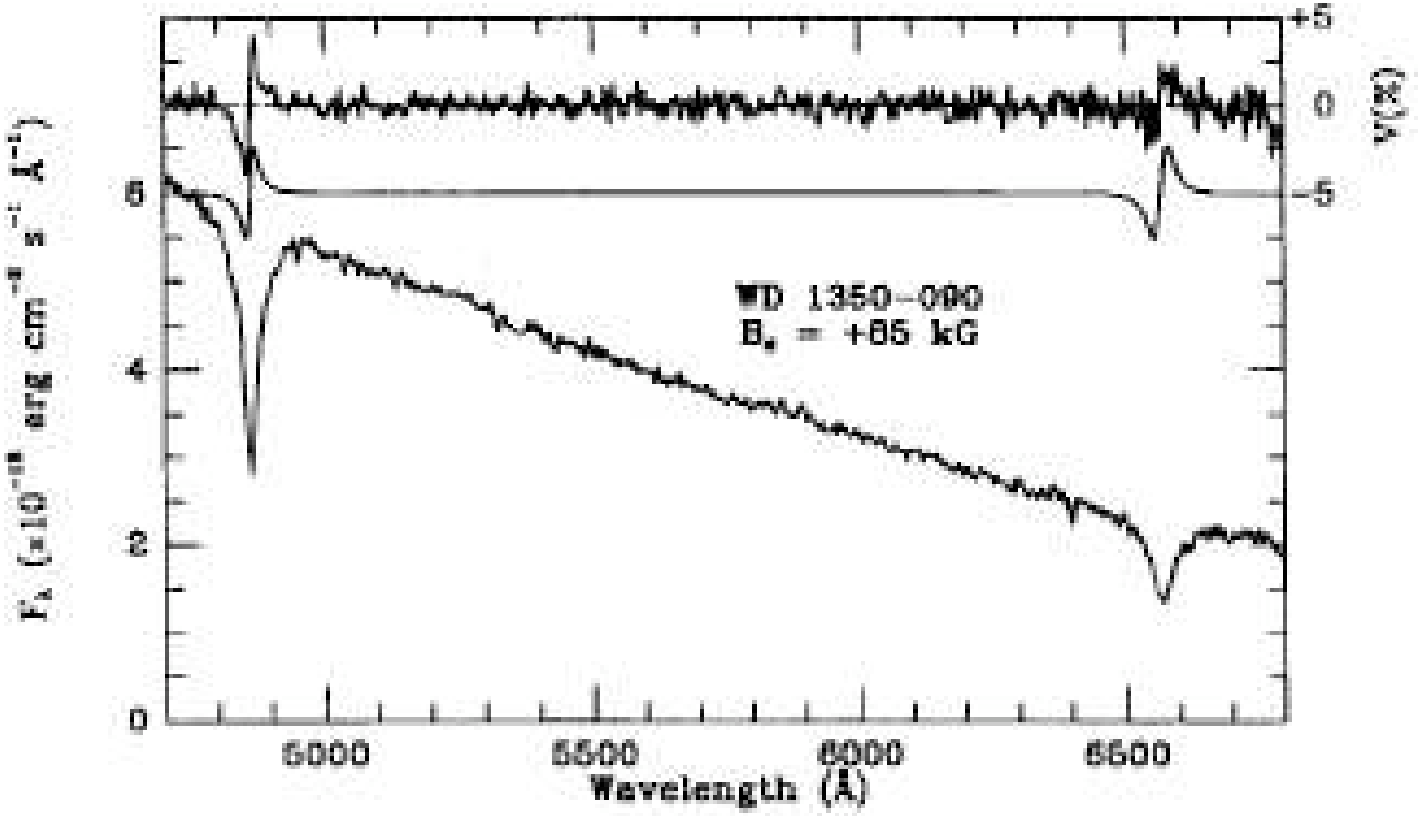


FIG. 4.—Intensity and circular polarization spectra of the low-field ($B = 85$ KG) white dwarf LP 907-037 (WD 1350−090). The $\sigma_-$ and $\sigma_+$ components are seen in left- and right-circularly polarized light but not in the intensity spectrum. A model polarization spectrum is also shown, offset by 5% in polarization for clarity (Schmidt & Smith 1994). Copyright *Astrophysical Journal*, reproduced with permission.

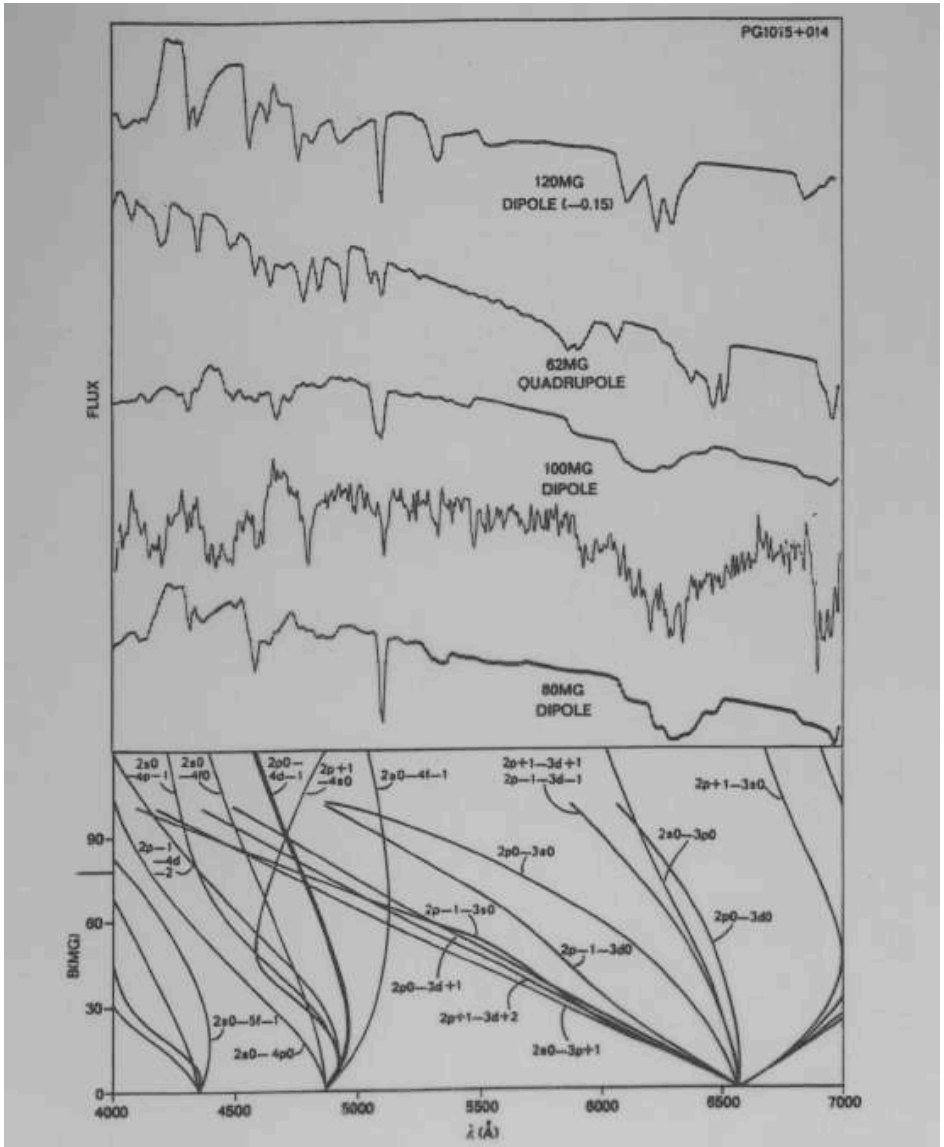


**Figure 5.** Lower panel: The magnetic field ($B$) and wavelength ($\lambda$) curves for H$\alpha$, H$\beta$ and H$\gamma$ transitions from Wunner *et al.* (1985) and Kemic (1974).

Upper panel: The flux spectrum ($F$, versus $\lambda$) at $0.0P$, compared with offset dipole, centred dipole and quadrupole models, for a viewing angle $\alpha=0°$, with respect to the magnetic axis. The zero flux level corresponds to that for the observed spectrum. The models are labelled with the dipole and quadrupole field strengths and have been scaled to match the observations at 5500 Å.

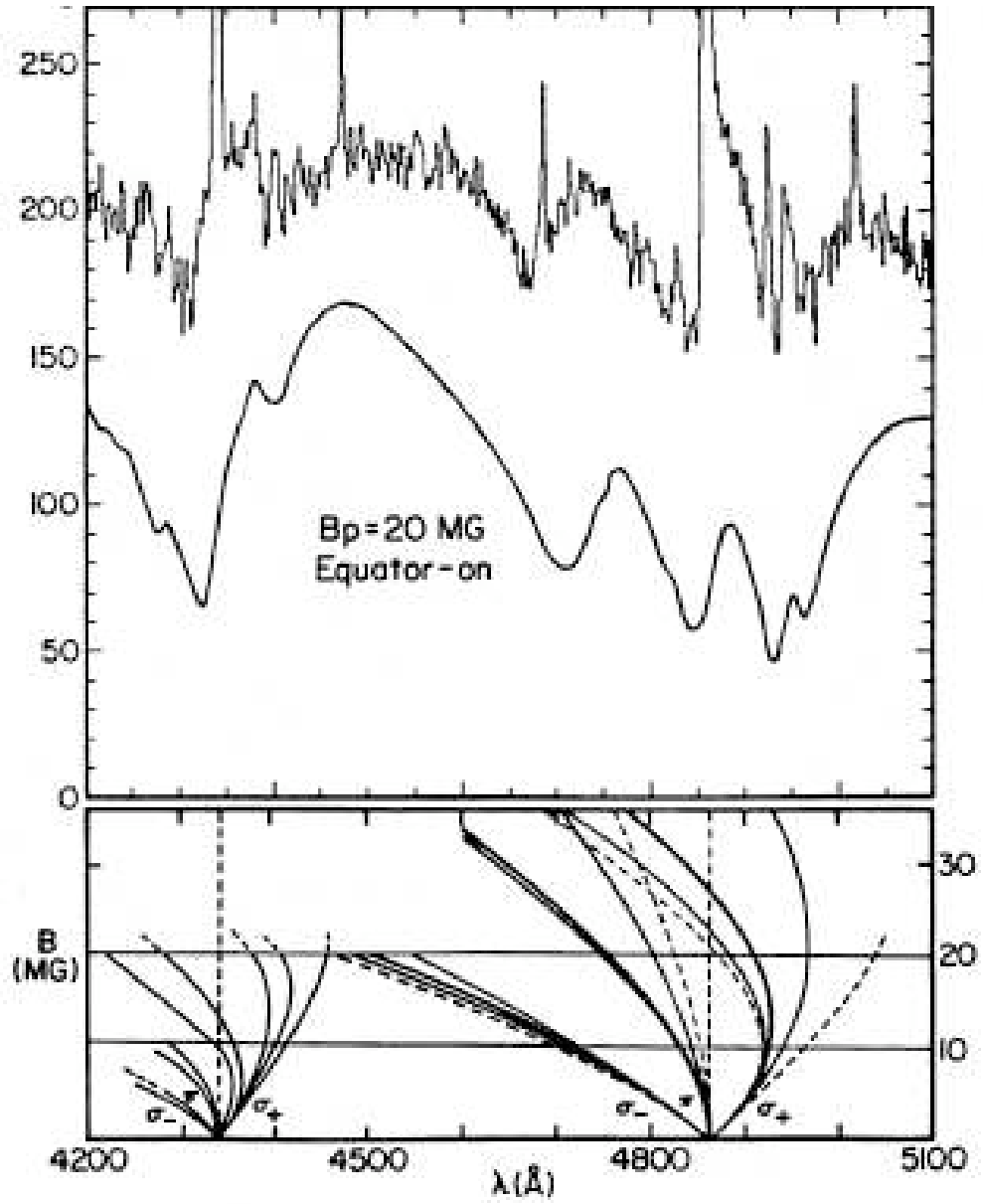
250
200
150
100
50
0
Bp=20 MG
Equator-on
B
(MG)
30
20
10
σ-
σ+
σ-
σ+
4200
4500
4800
5100
λ(Å)

| System | $B_{c1}$ (MG) | $B_{c2}$ (MG) | $\langle B_z \rangle$ (MG) | $B_H$ (MG) | $M_{WD}$ ($M_\odot$) | Period (minutes) | Notes | References |
|---|---|---|---|---|---|---|---|---|
| AR UMa (= 1ES 1113+432) | ... | ... | 230 | ... | ... | 116 | | 1, 2 |
| V884 Her (= RX J1802+18) | 120 | ... | ... | ... | ... | 113 | | 3, 4 |
| RX J1007−20 | 92 | ... | ... | ... | ... | 210 | | 5 |
| QS Tel (= RE J1938−461) | 70 | 47 | 38 | ... | ... | 140 | $a_z = 0.1$ | 6, 7 |
| RX J0132−65 | 68 | ... | ... | ... | ... | 78 | | 8 |
| RX J2022−39 | 67 | ... | ... | ... | ... | 78 | | 8 |
| V1309 Ori (= RX J0515+01) | 61 | ... | ... | ... | ... | 480 | | 9, 10 |
| DP Leo (= E1114+182) | 59 | 31 | ... | ... | 0.71 | 90 | $a_z = 0.1$ | 11, 12, 13, 14 |
| RX J1313−32 | 56 | ... | ... | ... | ... | 255 | | 15 |
| VV Pup | 56 | 31 | ... | ... | ... | 100 | $a_z = 0.1$ | 16, 17 |
| UZ For (= EXO 0333−25) | 56 | ... | ... | ... | $0.7^{+0.09}_{-0.09}$ | 127 | $a_z = 0.1$? | 18, 19, 20, 21 |
| 1RXS J1016.9−4103 | 52 | ... | ... | ... | ... | 122 | | 22, 23 |
| RX J1724+41 | 50 | ... | ... | ... | ... | 120 | | 24 |
| EK UMa (= 1E 1048+542) | 47 | ... | ... | ... | ... | 115 | | 25 |
| 1RXS J012851−23 (= RBS 206) | 45 | ... | 36 | ... | ... | 90? 146? | | 26 |
| EU Uma (= RE J1149+28) | 43 | ... | ... | ... | ... | 90 | | 27, 28 |
| EU Cnc (= G186) | 42 | ... | ... | ... | ... | 125 | | 29 |
| MN Hya (= RX J0929−24) | 42 | 20? | ... | ... | ... | 203 | $a_z = 0.1$ | 30, 31 |
| BY Cam (= H0538+608) | 41 | ... | ... | ... | ... | 202[a] | | 32 |
| RX J0803−47 | 39 | ... | ... | ... | ... | 137 | | 33 |
| RX J0203+29 (= EQ J0203+29) | 38 | ... | ... | ... | ... | 275 | | 34 |
| EV UMa (= RE J1307+535) | 37? | 30? | ... | ... | ... | 80 | | 35 |
| RS Cae (= RX J0453−42) | 36 | ... | ... | ... | ... | 94? 102? | | 36 |
| AN UMa (= PG 1101+453) | 36 | ... | 35 | ... | ... | 115 | | 32, 37 |
| HU Aqr (= RE J2107−051) | 36 | ... | 20 | ... | ... | 125 | | 38, 39 |
| MR Ser (= PG 1550+191) | 25 | ... | 27 | 25 | $0.62^{+0.23}_{-0.14}$ | 114 | | 37, 40, 41, 14 |
| RX J0501−03 | 25? | ... | ... | ... | $0.43^{+0.10}_{-0.07}$ | 171 | | 42 |
| V834 Cen (= E1405−451) | 23 | ... | 22 | 23 | ... | 101 | | 43, 44, 45 |
| BL Hyi (= H0139−68) | 23 | ... | 21 | 12 | ... | 114 | Complex | 46, 47, 48 |
| EF Eri (= 2A 0311−227) | 21 | 17 | ... | 15 | ... | 81 | Complex | 49, 50, 51 |
| V895 Cen (= EUVE J1429−38) | 20? | ... | ... | ... | ... | 286 | | 52 |
| UW Pic (= RX J0531−46) | 19 | ... | ... | ... | ... | 133 | | 53 |
| EP Dra (= H1907+690) | ... | ... | ... | 16 | ... | 105 | | 54 |

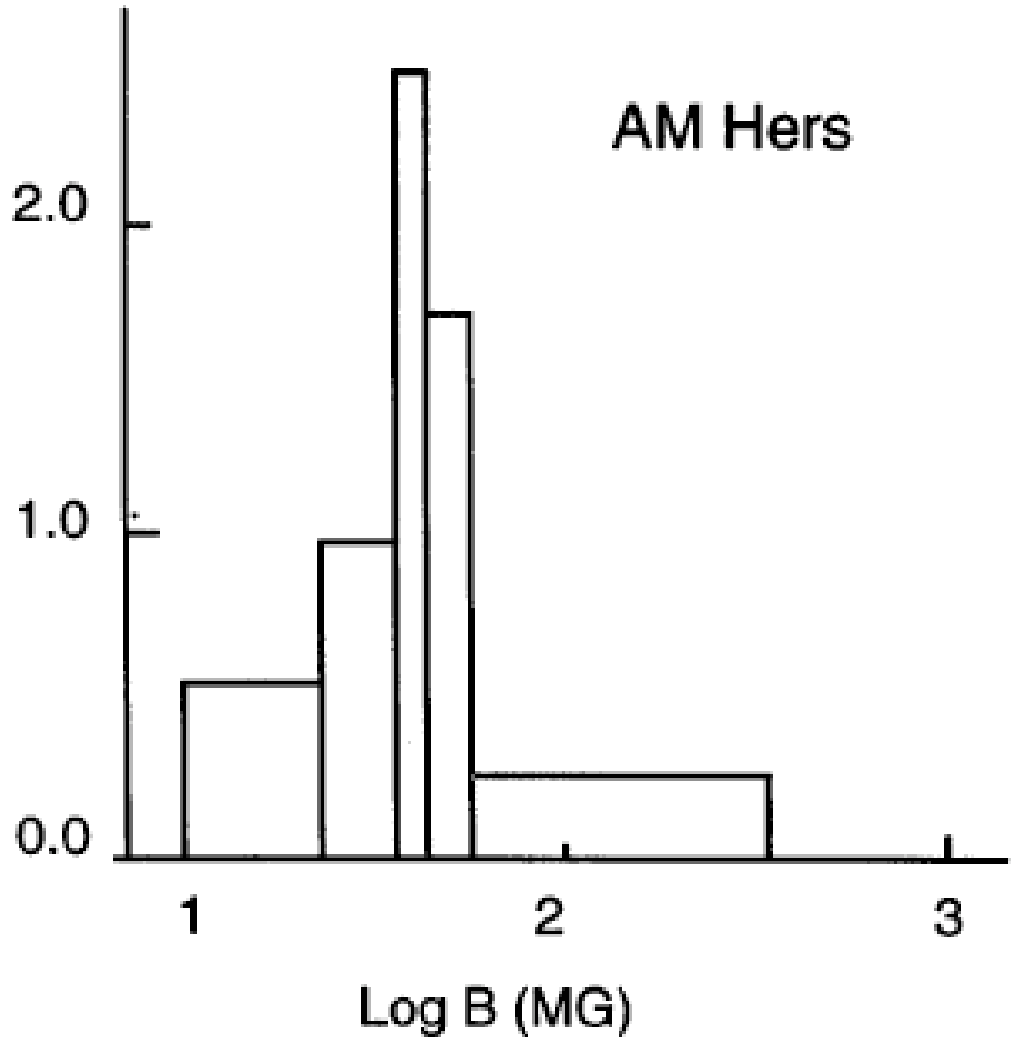


FIG. 39.—Normalized histogram of the field distribution of AM Hers in Table 2. Copyright *Astrophysical Journal*, reproduced with permission.

# Polars are X-ray factories

Infall energy per nucleon is

$$E_H = \frac{GM_1 m_H}{R_1} = 100\ (M_{1,0.6}/R_{1,9})\ \mathrm{keV}$$

A magnetic white dwarf will be a strong X-ray emitter (e.g., 3U 1809+50 = AM Herculis) if $\dot{m} \gtrsim 0.1$ g cm$^{-2}$ s$^{-1}$. X-rays originate in a radial shock.

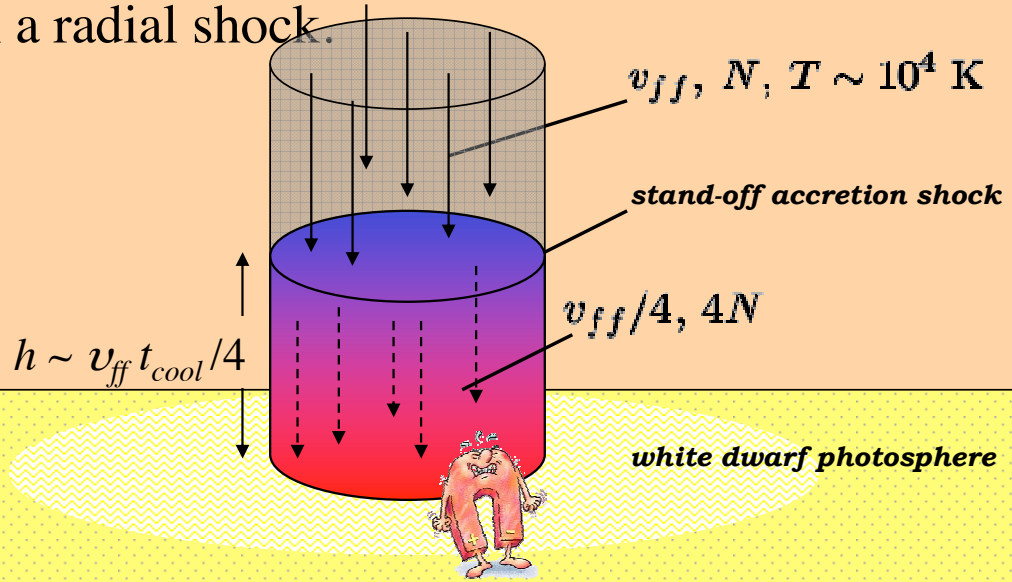

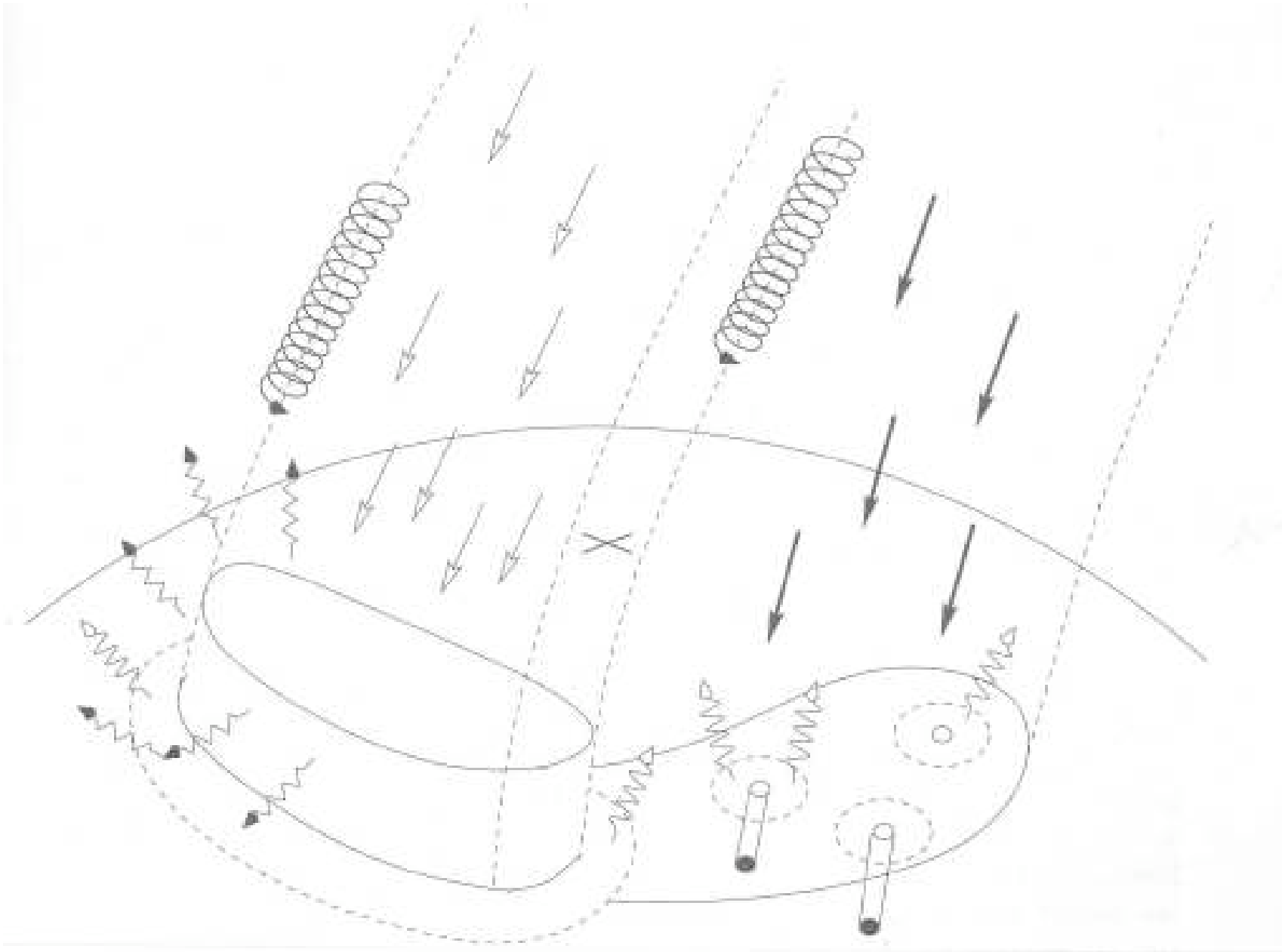

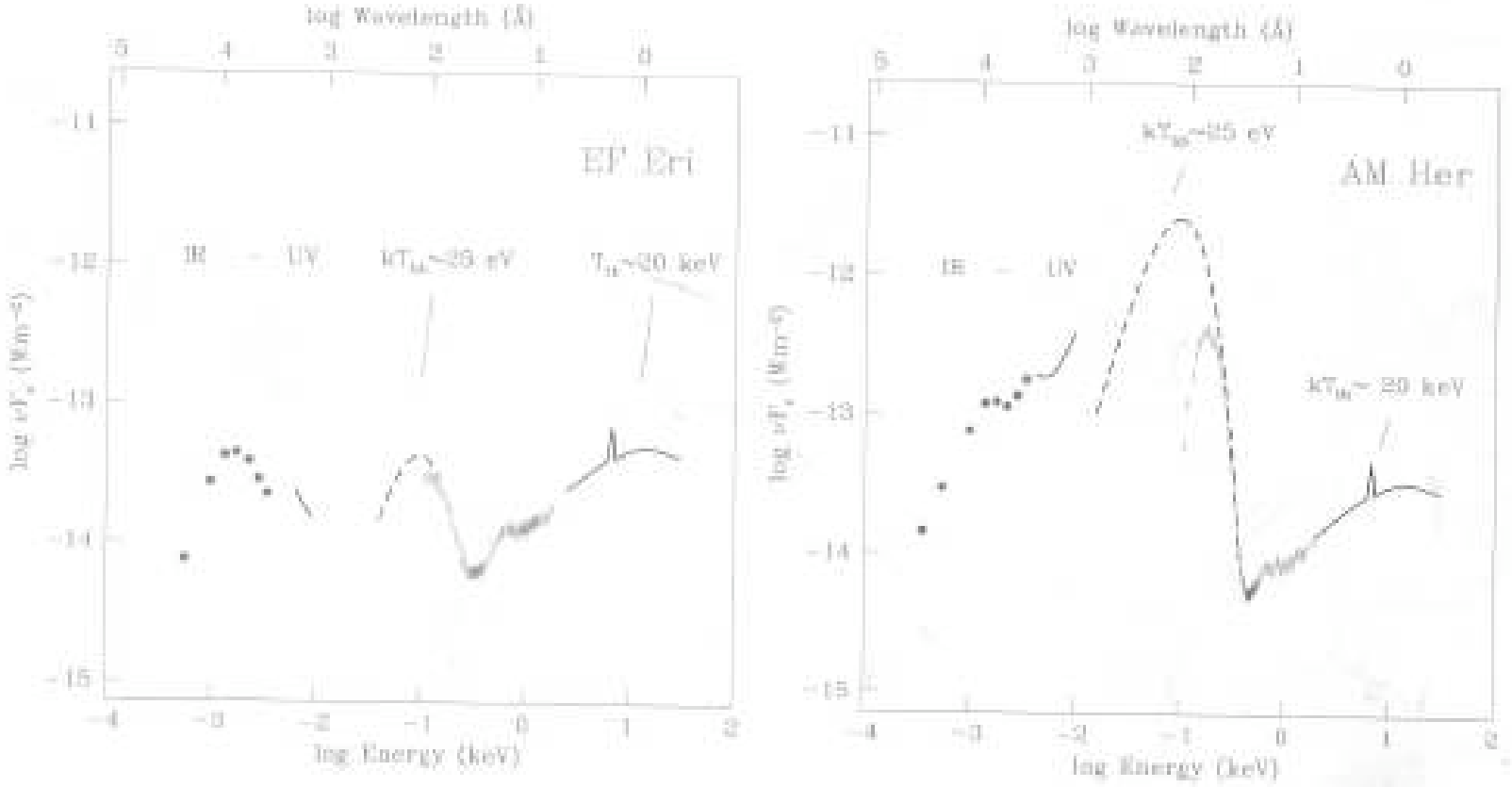


Fig. 8.11: Spectra of two AM Hers from the infrared to the hard X-ray, plotted as energy output versus photon energy. The three main components are (1) the hard bremsstrahlung emission from the accretion shock (which dominates at 1–100 keV); (2) soft-X-ray emission from blobby accretion and from reprocessing of harder X-rays (this dominates at 10–300 eV); and (3) the cyclotron emission in the optical and infrared. In EF Eri the three components emit similar amounts of energy, whereas in AM Her the soft-X-ray component is much larger, indicating that blobby accretion dominates the energetics. (Figures by Klaus Beuermann.[11])